First studies of a prototype GEM readout for a future ILC-TPC

Masterarbeit
zur Erlangung des akademischen Grades
Master of Science in Physics
(M.Sc.)

dem Fachbereich Physik der
Universität Siegen

vorgelegt von
Bakul Gaur

March 2008

Abstract

The world wide high energy physics community has been planning the next large particle collider after the Large Hadron Collider (LHC). It is called the International Linear Collider (ILC) and it will allow precision measurements refining any LHC findings. This requires very precise measurements of energy and momentum and high-resolution vertex reconstruction of the collision products. A time projection chamber (TPC) with pad readout is one of the favored choices for its central tracker. Physics goals and performance requirements of the ILC impose challenges for the detector technology. A new method for gas amplification is being studied in order to construct a TPC prototype for the ILC. The gas electron multiplier (GEM) is a promising technology for gas amplification. However, stable operation of a GEM-based detector and its optimization requires a good understanding of its behavior.
The present thesis describes the various hardware and software components that have been devised to successfully run a detector with pad readout. The detector uses a double GEM structure to achieve the necessary gas amplification. The pad readout is connected to a data acquisition (DAQ) system, that allows high-resolution sampling (4 ns) of the detector signals, using time interleaved flash analog-to-digital converters. The reconstruction of the signals, in order to obtain their rise time and fall time information, is discussed. An attempt was made to measure the signal sharing between adjacent pads. The results of the measurements are also discussed.

Contents

Chapter 1

Introduction

It has always been a human quest to explore the world around, and to probe deeper and deeper. Every discovery has a positive effect on our understanding of the universe. For example, the discovery of the electron in 1879 by J.J. Thomson, confirmed our beliefs about matter being formed of tiny structure-less particles. When the proton and the neutron were discovered, they were thought to be, like electrons, elementary. We now know that even the proton and the neutron have a complex structure. Our present understanding of these, and of many other particles discovered since, and their interactions with each other, is best described by the standard model (SM) of particle physics.

1.1 The Standard Model

The standard model of particle physics is, at the time being, the mathematical formulation that best describes the experimental data. According to the model, the matter around us is made up of elementary fermions, namely, quarks and leptons. There are other fermions that do not occur that often, and are only seen in cosmic-ray or high energy physics experiments. These are categorized into three generations based on their masses and stability (Fig. 1.1)[1]. The first generation particles are the most stable and the least massive of all. The unstable second and third generation particles, however, decay into the first generation particles. Each lepton has a neutrino associated with it, for example, the electron (e), the electron-neutrino (ν_e). Further, for each elementary fermion there exists an antiparticle with the same properties, but opposite charge.

The model also explains the various forces that exist in nature, by means of force carrier particles or exchange bosons. These bosons mediate the interactions between the other elementary particles and are the signature of that interaction. For the electromagnetic case, the force is carried by photons (γ). Similarly, the weak interactions are mediated by the charged W-bosons (W^-,W^+) and the neutral Z-boson (Z^0); and the strong interactions are mediated by the gluons (g). At the level of particle physics the gravitational force is insignificant, and the SM does not include this force.

All fermions have spin $\frac{1}{2}$, in units of $\hbar$. They obey Fermi-Dirac statistics and the

Pauli exclusion principle. Quarks have fractional elementary charges and they do not exist on their own, but they form other composite particles. The up (u), charm (c) and top (t) quarks have charge $\frac{2e}{3}$ (where e is the elementary charge), while the down (d), strange (s) and bottom (b) quarks have charge $\frac{-e}{3}$. Quarks and gluons also have an interesting property called the color-charge (see, for example, [2, 3]). The strong interactions of the quarks and gluons are described by the theory of quantum chromodynamics (QCD)[1]. Baryons are three quark systems such that the charge quantization is not violated and they are color-neutral, for example, the neutrons $(udd)^0$ are charge-less and the protons $(uud)^+$ bear a positive charge. Mesons consist of a quark-antiquark pair and are all unstable. For example, the least massive mesons are pions (π^-,π^0,π^+). Mesons and baryons are, collectively, called hadrons. Bosons are particles with integer spin and they obey Bose-Einstein statistics. In contrast to fermions, they may share the same quantum states. Their wavefunctions are symmetric, i.e. an exchange of indistinguishable bosons does not change their wavefunctions [4]. Pions are examples of composite bosons.
All of the elementary bosons, except the W and Z bosons, are mass-less. The fact that the W and Z bosons have masses can be explained well by introducing the existence of an isodoublet scalar field and a corresponding particle called the Higgs particle [1]. It should be noted, that this is just a theoretical concept and the particle itself has never been observed. Although there are different assumptions concerning the mass of the Higgs particle, its lower limit is estimated to be $\sim 114.4\,\mathrm{GeVc}^{-2}$ [5]. The Higgs has spin zero and therefore it is also a boson.
The SM may have been very successful, but there are some problems with it. There is no quantum theory that describes gravity. There exists a hierarchy problem: the SM does not explain why particle masses are so small compared to the Planck mass. It does not clarify why the neutrinos may have masses, and why there are only three generations of fermions. There are many more unanswered questions (reference [1] has more details).

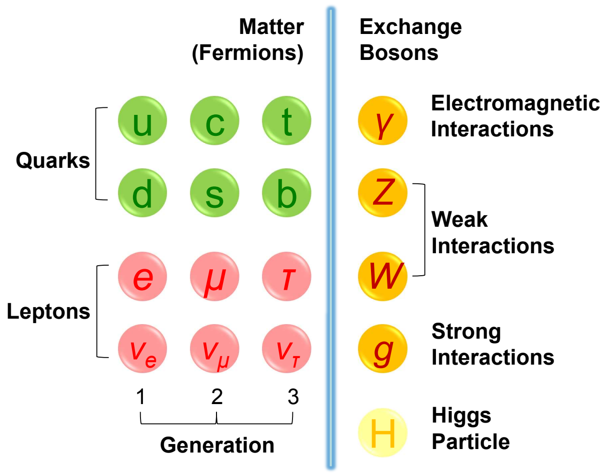

Figure 1.1: The standard model particles: the elementary fermions, their generations, and the exchange bosons. The existence of the Higgs particle has not been confirmed yet.

1.2 Beyond the Standard Model

It would be much nicer, if there was one theory that described everything. For example, the quantum electrodynamics (QED), is one theory that describes all the electromagnetic phenomena around us. The Glashow-Weinberg-Salam theory [6, 7, 8] combines the weak and the electromagnetic forces. Particle physicists are striving for a grand unification theory (GUT) which may combine the electro-weak and the strong forces (Fig. 1.2). Further, a theory that combines all the four forces together (including gravitation), may help us understand the condition of the early universe. Since the SM has been very successful so far, most likely it will not be replaced by another model, but extended. The supersymmetry (SUSY) model is such an extension, which is very promising. It assumes a supersymmetric counterpart for every elementary particle (i.e. for each particle shown in fig. 1.1). The discovery of either the Higgs, or any of the SUSY particles, or both, will help build the model further [1].

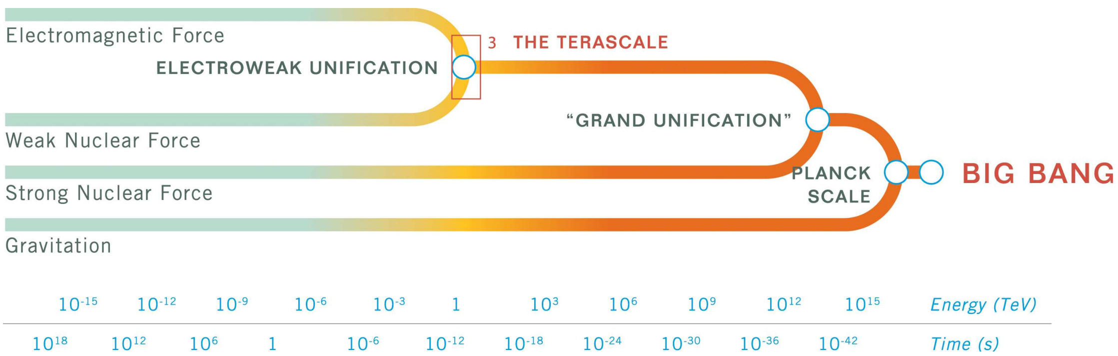

Figure 1.2: Unification of all forces [9].

1.3 Motivation to Build a Detector Prototype

The large electron-positron collider (LEP) was one of the world's largest synchrotron colliders at CERN[1] which operated at a center-of-mass energy of $\sim 200\,\text{GeV}$. The energy loss per particle per turn at a synchrotron accelerator is $\Delta E \sim 1/m_0^4$, where m_0 is the rest mass of the particle [4]. Hence, the smaller the particle mass, the larger the energy lost per turn. The maximum achievable energy at LEP was limited due to synchrotron radiation losses. However, it was very successful in testing the SM to a good precision. Now, it has been replaced by the large hadron collider (LHC). It is a proton-proton accelerator, and it can provide 14 TeV center-of-mass energy. A proton's mass is much larger than that of an electron and hence it can be accelerated to much higher energies, but there are other problems in dealing with protons, for example, large QCD background in the detector and indefinite initial

[1]Conseil Européen pour la Recherche Nucléaire (CERN), the European particle physics laboratory in Geneva, has been providing particle accelerators and detectors for physics experiments since many decades.

states of the colliding particles, since they are composite particles. If there are any Higgs or SUSY particles, there is a good chance, that the various experiments at the LHC will detect them and determine their masses (see, for example, [10]). However, to perform a complete analysis of the Higgs and SUSY particles (if they are discovered), a much higher precision machine is required.

The worldwide high energy physics community has decided to build the international linear collider (ILC) that will be based on superconducting radio-frequency linac (SCRF)[2] technology. It will collide electrons and positrons, initially, at 500 GeV center-of-mass energy, and later, at $\sim$ 1 TeV (Fig. 1.3). Besides the advantage of a cleaner environment (smaller background), there are many other interesting possibilities, for example, the electron and positron beams can be polarized and the ILC can be used as an electron-photon or photon-photon collider [12].

Physics goals and performance requirements of the ILC impose challenges for the detector technology. The detector must be as hermetic as possible. The energy and the momentum of the produced particles must be very precisely measured. The reconstruction of decay vertices is very important for particle identification. This requires efficient pattern recognition even in presence of background, and therefore a high resolution vertex detector [13].

This thesis describes the experimental setup of a TPC prototype as a tracking detector for the ILC. The objective is to study the gas amplification mechanism and the readout system and their optimization.

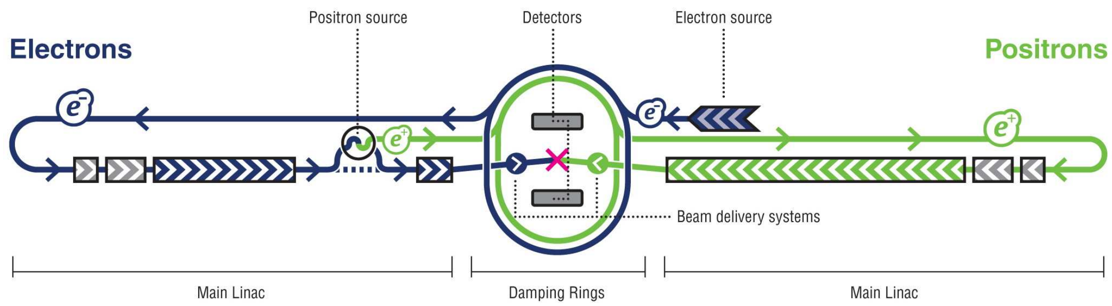

Figure 1.3: The international linear collider: it will use 9-cell 1.3 GHz superconducting niobium cavities (17,000 total cavities) to accelerate electrons and positrons. It will be $\sim$ 31 km long and shall provide 200-500 GeV center-of-mass energy at $500 - 1000\,\mathrm{fb}^{-1}$ luminosity [12].

[2]SCRF linac technology was pioneered by the TeV-energy superconducting linear accelerator (TESLA) collaboration at Deutsches Elektronen-Synchrotron (DESY) [11].

Chapter 2

Detector Physics

This chapter briefly discusses the physics involved and the working principles of the detectors used in the work presented here. More emphasis is given to the gas amplification mechanism of the GEMs, which is discussed at the end.

2.1 Interaction of Particles with Matter

When charged particles traverse a gaseous medium, they loose their energy due to ionization and excitation. They knock off electrons from the atoms of the medium, producing electron-ion pairs along their trajectories. Some of these primary produced electrons have enough energy to produce further (secondary) ionizations on their own. Hence, the ionizing particles leave several charge clusters behind. The specific energy loss of an ionizing particle is given by the Bethe-Bloch formula [14, 15, 16, 17, 18]:

$$-\frac{\mathrm{d}E}{\mathrm{d}x} = 4\pi N_{\mathrm{A}} r_e^2 m_e c^2 z^2 \frac{Z}{A}\frac{1}{\beta^2}\left[\ln\frac{2m_e c^2\gamma^2\beta^2}{I} - \beta^2\right], \tag{2.1}$$

where

z	is the charge of the ionizing particle,
Z, A	are the atomic and the mass numbers of the gas,
m_e	is the electron mass,
c	is the velocity of light,
r_e	is the classical electron radius ($r_e = \frac{1}{4\pi\epsilon_0}\frac{e^2}{m_e c^2}$), where e is the charge of an electron and ϵ_0 is the permittivity of free space,
N_{A}	is the Avogadro number,
I	is the ionization constant, approximated by $I = 16Z^{0.9}$ eV for $Z > 1$,
β	is the ratio of the velocity of the ionizing particle to that of light (c),
γ	is the Lorentz factor ($\gamma = \sqrt{1/(1-\beta)^2}$).

For lower energies of the ionizing particles, the $1/\beta^2$ term in equation 2.1 dominates, and the energy loss decreases (as energy increases) up to a minimum value (see fig. 2.1). The minima correspond to $\gamma \approx 4$ and the particles having such energies are called "minimum ionizing particles". For higher energies, i.e. $\gamma > 4$, the logarithmic term in equation 2.1 dominates, and the energy loss increases until a plateau is reached. Notice that the $\frac{\mathrm{d}E}{\mathrm{d}x}$ curve for the electrons is quite different from that of the other charged particles (see fig. 2.1). The Bethe-Bloch formula applies only to particles heavier than the electrons. It describes the mean energy loss of the charged particles. The energy loss fluctuations are Landau distributed. The measurement of the particles' momenta and the energy loss $\frac{\mathrm{d}E}{\mathrm{d}x}$ in a detector can be used to identify the particle species.

Charged particles having masses comparable with the mass of an electron undergo bremsstrahlung energy losses (in addition to ionization and excitation), when they are decelerated in the Coulomb field of the gas nuclei. A fraction of their energy is emitted in form of photons. The bremsstrahlung energy loss of electrons is given by:

$$-\frac{\mathrm{d}E}{\mathrm{d}x} = \frac{E}{X_0}, \tag{2.2}$$

where X_0 is called the radiation length of the ionizing medium.

The photons are either completely absorbed in the gas medium, or are scattered by quasi-free atomic electrons (Compton scattering). The absorption of the photons at lower energies ($< 100\,\mathrm{keV}$), is dominated by the photoelectric effect. For this, the photons must have energies greater than the binding energy of the gas atoms. Their excess energies are carried by the electrons liberated in the process. For photon energies of about $1\,\mathrm{MeV}$ the main process is the Compton scattering process. In this process the photons are scattered by quasi-free atomic electrons of the gas medium, and only a fraction of the photons' total energy is lost to the electrons. For higher energies ($\gg 1\,\mathrm{MeV}$), the dominating process is the electron-positron pair-production due to the photon's interaction with the Coulomb field of the atomic electrons or the nuclei [19, 20].

2.2 Drift and Diffusion in Gases

The electrons and the ions produced in a gas due to the processes described above have a thermal motion. They loose their energy by repetitive collision with the other atoms and molecules. On application of an electric field, they acquire a net motion in a direction that is parallel to the field. The drift velocity can be expressed as:

$$v_{\mathrm{d}} = \mu E \frac{p_0}{p}, \tag{2.3}$$

where μ is the charge carrier mobility, E is the applied electric field, and $\frac{p_0}{p}$ is the pressure normalized to the standard pressure.

The drift velocity of the electrons in argon based gas mixtures is of the order of a few cm/μs. It increases with the applied electric field until it reaches an almost constant value ($\sim 5\,\mathrm{cm}/\mu\mathrm{s}$, at an electric field of about $1000\,\mathrm{V/cm}$, in Ar-CO_2 [21]). This region is particularly important for the operation of the gas detectors, as the drift velocity remains more or less constant for a range of electric fields.

The collisions of the charge carriers with the atoms and the molecules of the gas

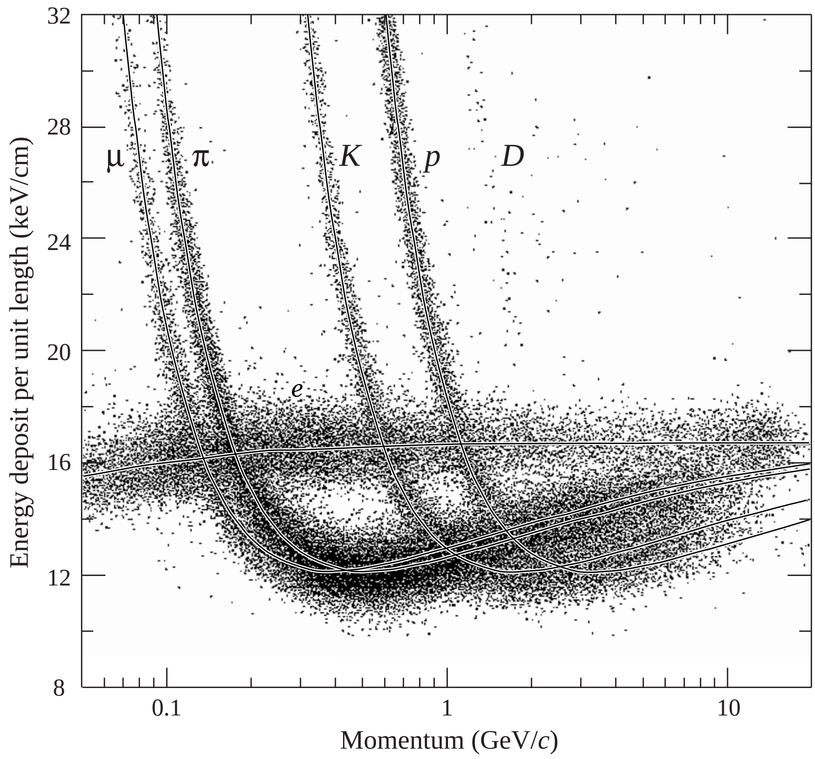

Figure 2.1: Specific energy loss of different charged particles: electrons (e), muons (μ), pions (π), kaons (K), protons (p) and deuterons (D), in Ar-CH_4 mixture [1].

lead to their diffusion. The diffusion is equal in all directions and is described by a Gaussian distribution:

$$n = \left(\frac{1}{\sqrt{4\pi Dt}}\right)^3 \exp\left(\frac{-r^2}{4Dt}\right), \tag{2.4}$$

where n is the density of the charge carriers, at a distance r away from the point of ionization after a time t, and D is the diffusion coefficient. The factor $\sqrt{2Dt}$, gives the width of the charge distribution, which develops with time. The diffusion coefficient is given as:

$$D = \mu\frac{kT}{q}, \tag{2.5}$$

where k is the Boltzmann constant, T is the temperature of the gas and q is the charge of the carrier.
The mobility μ is expressed as:

$$\mu = \tau\frac{q}{m}, \tag{2.6}$$

where m is the mass of the charge carrier, and τ is the collision rate. τ depends on the mean free path of the charge carriers in the gas. The mobility μ is different for the electrons and the ions. In general, the mobilities of the electrons in gases are about three orders of magnitude higher than those of the ions [22, 23].

2.3 Fe^{55} Spectrum

An Fe^{55} source predominantly emits X-rays of 5.89 keV energy. In gaseous Argon the X-ray photons are absorbed by the photoelectric effect. The kinetic energy of the produced photo-electrons is the difference between the photon's energy and the binding energy (3.19 keV) of the K-shell electrons in Argon, i.e. 2.70 keV. The vacancy created in an Argon atom, due to the emission of a photo-electron, is filled by another electron from its higher energy levels. This leads to either the production a photon (characteristic X-rays of Argon), or an Auger electron (Auger effect). Both, the photo and the Auger electrons, loose their energy by ionization, to produce electron-ion pairs as described in section 2.1. The number of the electron-ion pairs produced is proportional to the energy of the ionizing electrons, i.e. ~ 227 pairs (ionization energy of Argon is 26 eV). The characteristic X-ray photons of Argon have energies slightly lower than the K-shell binding energy. Hence, they are not re-absorbed and they escape the detector. In this case electrons-ion pairs produced are only due the photo-electron (~ 123 pairs).
The resulting pulse height spectra have two distinct peaks. The higher peak corresponds to the 5.89 keV energy and the smaller corresponds to the 3.19 keV energy. The smaller is called the Argon-escape peak.

2.4 Proportional Counters

As described in section 2.3, the number of electron-ion pairs produced by ionization is about a few hundred. Amplification is generally required to produce a signal large enough that can be handled by the electronics. Different detectors use different methods for charge amplification (section 2.7 describes one). In most cases the amplification is performed, such that the resulting signal is proportional to the initial ionization.
Particle detectors often use electric fields to collect ionization products on their electrodes, in order to obtain a signal. By suitable application of electric fields, the drifting electrons can be given enough energy to produce ionization on their own. For example, section 3.3.3 describes the proportional tube used in the experimental setup. A proportional tube consists of a thin wire, stretched at the center of a conducting tube, at a high electrostatic potential compared to the tube. The electric field intensity inside the tube increases as $\frac{1}{r}$ (where r is the radial distances from the center). At a point where the field exceeds a critical value (several kV/cm), the electrons ionize and multiply to produce an avalanche. It produces a signal proportional to the energy of the initial ionization. If the gas density is more or less stable, the gas gain can be assumed to be constant. However, the local variations of the gas gain owing to factors like mechanical imperfections of the detector, voltage variations, etc., lead to a Gaussian like distribution of the pulse height spectra. A more detailed discussion of proportional detectors is beyond the scope of this chapter. The signal development and the gain calculation are discussed in literature, e.g. [24, 19, 23].

2.5 Drift Chambers

Although there exists a large variety of drift chambers used in particle physics experiments [22], this and the next sections briefly describe their basic principle of operation in the context of the work presented here.
A drift chamber is an ionization detector, which is used to determine the spatial coordinates of the ionizing event. The ionization can be point like, or a series of points that form a particle's trajectory. The detector essentially consists of a drift cathode that provides a drift field to bring the charge clusters produced in the detector to the readout electrodes. A suitable gas is filled inside the detector, to provide a medium for ionization and charge carrier transport. Every drift chamber has some means of achieving gas amplification. Although not necessary, field shaping electrodes can be placed along the drift direction to provide a uniform drift field.

2.6 Time Projection Chambers

The conventional drift chambers provide two-dimensional coordinate measurement. However, if the arrival time of the ionizing particle and the drift velocity are precisely known, the third coordinate can be calculated. This principle is employed in a special class of drift chambers called time projection chambers (TPC). The TPCs have comparatively large drift volumes. To minimize the effects of diffusion, they are often subjected to high magnetic fields parallel to the drift direction. They have, additionally, a gate mash between the drift region and the gas amplification region. Its purpose is to prevent ions produced during gas amplification from entering the drift region. Otherwise, the ions deteriorate the drift field. The gate is kept at a negative potential compared to the gas amplification devices and it is only disabled for a short time period after an event takes place in the drift space.

2.7 Gas Electron Multipliers

Gas electron multipliers (GEMs) are gas amplification devices, essentially consisting of two fine copper foils separated by a polyimide foil[1], with a high density of holes [25]. Fig. 2.2(a) shows a photograph of a GEM (see also fig. C.1 in appendix C for the geometry details of the GEMs used in the work presented here). This section describes the working principle of a double-GEM structure.
Since the upper and the lower surfaces of the GEMs are identical, the choice of cathode or anode is only a question of the applied voltages. Typically a potential difference of 300 V to 400 V is applied across the GEMs. The thickness of the polyimide foil is about 50 μm, and hence the electric fields between the GEM holes can be of the order of several tens of kV/cm. The hole electric field can be calculated as [26]:

$$E_{\text{hole}} = a\Delta V_{\text{GEM}} + b(E_{\text{top}} + E_{\text{bottom}}), \tag{2.7}$$

[1]Kapton film, developed by DuPont.

where a and b are GEM geometry dependent constants and E_{top} and E_{bottom} are the fields above and below a GEM, respectively.
When ionizing particles traverse the drift region (see fig. 2.2(b)), electron-ion pairs are created. In the presence of the electric field the electrons drift towards the pad plane (anode). Near the GEM surface (GEM cathode), most of the field lines collect into the GEM holes and emerge on the other side (transfer region), while the others may terminate on the GEM cathode itself, as demonstrated in fig. 2.2(b) (see reference [25] to get a better picture of the field lines around GEMs). The electrons follow the field lines and therefore they either pass through the holes (collection) or are lost to the GEM cathode. The collection of the electrons into the holes takes place due to the focusing effect of the field lines. Inside the holes, they gain energy due to the high electric field and create further electron-ion pairs by subsequent collisions with the gas molecules (within the confines of the holes). The ions drift back into the drift region while the electrons are extracted into the transfer region (for a single GEM setup this is the induction region). Not every field line emerging out of the holes goes all the way to the next GEM. Some of them terminate on the anode surface of the same GEM instead. A similar process takes place inside the other GEM creating more electrons and ions. Thus amplification is increased as many times as there are GEMs.
The transfer and the drift regions have both electron and ion currents, while the induction region has only an electron current. By suitably setting the GEM voltages, not only higher gas amplifications can be achieved, but also the ion back drift can be minimized [27], thus eliminating the need for a gate in the detector.

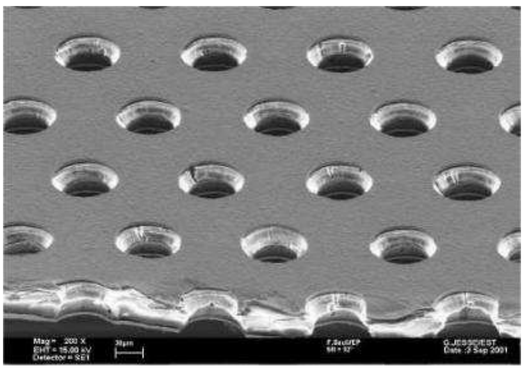

(a)

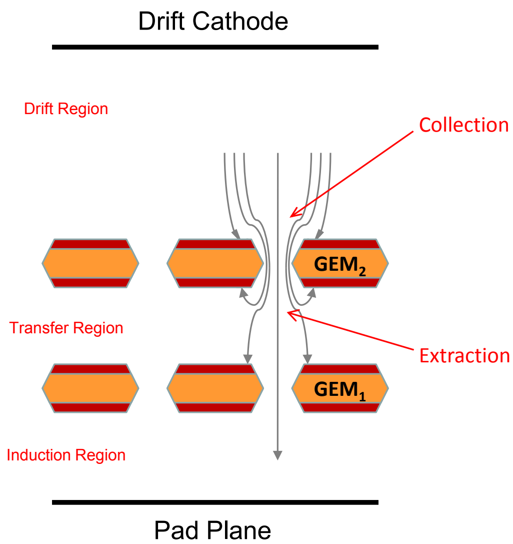

(b)

Figure 2.2: Gas electron multipliers: (a) shows a scanning electron microscope photograph of a GEM [28]. (b) shows an abstract diagram of a two GEM detector showing the drift, the transfer and the induction regions. The diagram also shows the collection and the extraction phenomena. The diagram and the field lines are not to scale (see reference [25] for more details).

2.7.1 Charge Transfer Coefficients

The overall gain of a GEM depends on the collection and extraction processes described above. Hence, they must be considered in order to compute the gain. The next few paragraphs describe them in more detail. The expressions and parameterizations introduced here are results of simulation studies described in references [26, 29, 27].

Collection Efficiency The electron collection efficiency is defined as the ratio of the number of electrons collected in the holes to the total number of electrons incident on the GEM surface. It depends on the ratio of the external electric field to the hole field ($\frac{E_{\text{top}}}{E_{\text{hole}}}$):

$$C^{-}_{\text{GEM}}\left(\frac{E_{\text{top}}}{E_{\text{hole}}}\right) = \begin{cases} 1, & \text{if } \frac{E_{\text{top}}}{E_{\text{hole}}} \leq r^{1/s} \\ r\left(\frac{E_{\text{top}}}{E_{\text{hole}}}\right)^{-s}, & \text{if } \frac{E_{\text{top}}}{E_{\text{hole}}} > r^{1/s} \end{cases}, \quad (2.8)$$

where r and s are free parameters [26].
The collection efficiency is also defined for ions, in which case the external electric field is the field below the GEM (E_{bottom}).

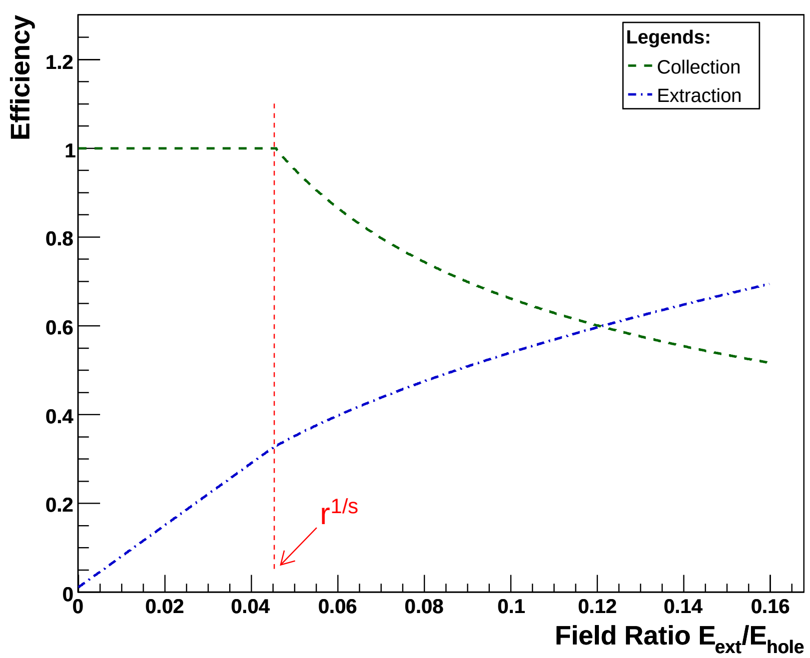

Figure 2.3: Electron collection and extraction efficiencies as a function of field ratio and their dependence on the factor $r^{1/s}$ [26, 27].

Extraction Efficiency The electron extraction efficiency is defined as the ratio of the number of electrons extracted from the GEM to the total number of electrons in the holes. It depends on the optical transparency of the GEM and the ratio of the external electric field to the hole field ($\frac{E_{\text{bottom}}}{E_{\text{hole}}}$). The optical transparency can be deduced from the GEM's geometrical parameters:

$$T_{\text{opt}} = \frac{\text{open area of the holes}}{\text{total foil area}} = \frac{\pi}{2\sqrt{3}} \left(\frac{d}{P}\right)^2, \tag{2.9}$$

where d is the diameter of the hole and P is the pitch. The extraction efficiency is:

$$X_{\text{GEM}}^{-}\left(\frac{E_{\text{bottom}}}{E_{\text{hole}}}\right) = \begin{cases} \frac{1}{T_{\text{opt}}}\left(\frac{E_{\text{bottom}}}{E_{\text{hole}}} - y\right) + g, & \text{if } \frac{E_{\text{bottom}}}{E_{\text{hole}}} \leq r^{1/s} \\ \frac{1}{T_{\text{opt}}}\left(\frac{E_{\text{bottom}}}{E_{\text{hole}}} - y\right)^{1-s} + g, & \text{if } \frac{E_{\text{bottom}}}{E_{\text{hole}}} > r^{1/s} \end{cases}, \tag{2.10}$$

where r, s, y and g are free parameters [27].
For ions, there are primary and secondary extraction processes. See reference [27] for details.

Gain The gain of a GEM is defined as the ratio of the number of electrons in the holes to the number of those collected before gas amplification. The gain increases exponentially with the potential difference across the GEM, ΔV_{GEM}. Hence, the gain is:

$$G_{\text{GEM}}^{-} = \beta e^{\alpha \Delta V_{\text{GEM}}}, \tag{2.11}$$

where α and β are free parameters.
Unlike the collection and the extraction efficiencies, the gain is only defined for electrons, not for ions.

Effective Gain As mentioned earlier, the three charge transfer coefficients affect the overall (effective) gain of a GEM. Hence, the effective gain of the GEM is expressed as a product of the three:

$$G_{\text{GEM}} = C_{\text{GEM}}^{-} X_{\text{GEM}}^{-} G_{\text{GEM}}^{-}. \tag{2.12}$$

Parallel Plate Gain The parallel plate gain is defined as the ratio of the number of electrons incident on a GEM surface (or the pad plane) to the number of those that were extracted from the adjacent GEM. This happens only if the transfer or the induction fields are about 6 kV/cm or above this value. Normally, such high fields between GEMs are not used and the parallel plate gain can be neglected.

Total Effective Gain The total effective gain of a multi-GEM assembly (say, an assembly of n GEMs) is a product of effective gains and parallel plate gains of each of the GEMs:

$$G = \prod_{i=1}^{n} G_{\text{GEM}_i} P_{\text{GEM}_i}. \tag{2.13}$$

Chapter 3

Experimental Setup

This chapter describes the experimental setup in detail. A high-level setup diagram is shown in fig. 3.1. The foremost component of the setup is a detector that uses GEMs for gas amplification and has a pad readout. Although the detector is meant to be a TPC prototype, the present thesis focuses on a test chamber that is used to understand the optimum settings required for stable operation of the detector.
The chapter also discusses the various devices that have been built to run the test chamber. There is a gas system that provides a drift gas mixture to the chamber. The gas mixture can be a standard Ar-CO_2 mixture from a gas bottle, or a custom mix based on an experiment's requirement. The gas system monitors the gas quality throughout an experiment and stores the necessary information for later review. A HV system provides the necessary high voltages to the various electrodes inside the chamber. The chamber's readout electronics comprise of many pre-amplifier channels. These channels are read by a DAQ system and the data is saved for later analysis. Most of these systems have been built such that they can also be used with the TPC prototype.

3.1 The Test Chamber

The test chamber is a drift detector. It uses a 2-GEM structure for gas amplification. The readout is performed using a segmented pad plane. The next few sections describe the various components of the test chamber.

3.1.1 Mechanical Assembly

The test chamber's mechanical assembly is as shown in fig. 3.2. All parts of the chamber are mounted on a printed circuit board (PCB). The PCB holds the GEM-cathode stack directly on top of the pads by means of plastic screws. It has points where the GEM and the cathode HV terminals are soldered. These points connect to the HV cables through $20\,\mathrm{M\Omega}$ resistors. The resistors and the cable connectors are covered by the black boxes shown in fig. 3.2(a).
The GEM foils are glued to $1\,\mathrm{mm}$ thick flame retardant-4 (FR-4) frames. The geometry of these GEMs was discussed in chapter 2. The cathode is a $7\,\mu\mathrm{m}$ thick

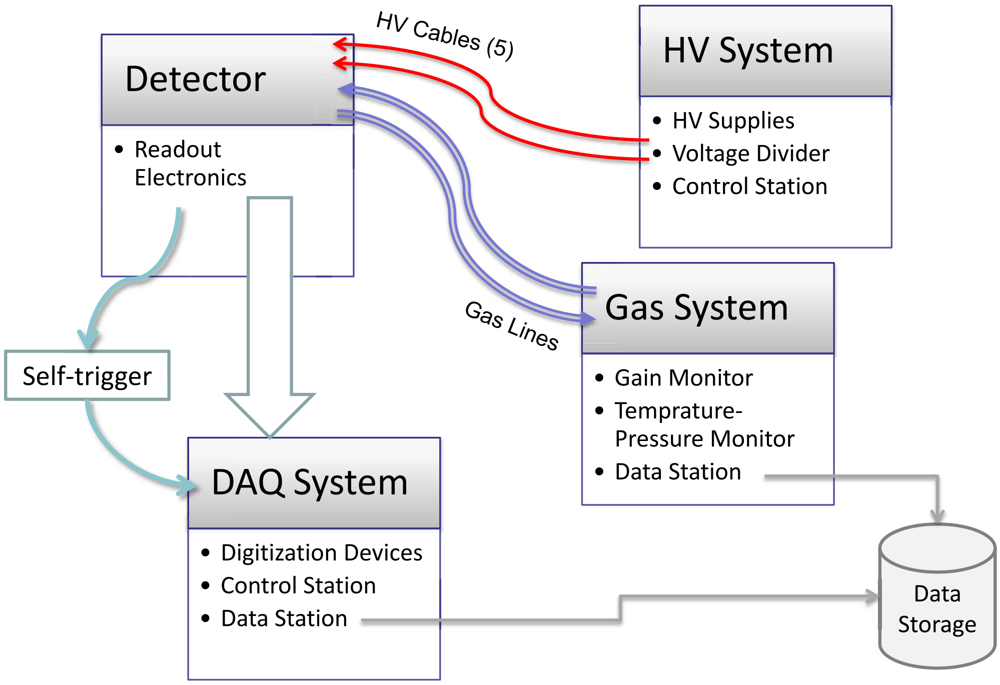

Figure 3.1: The main components of the experiment: the detector is a test chamber containing two GEMs, a cathode and a pad plate. The readout electronics amplifies the signals from the pads and delivers them to the DAQ system. Five HV cables connect the GEMs and the cathode to the HV system. A gas lines brings a gas mixture to the detector and another line returns it back to the gas system (exhaust).

polyester foil[1] with a thin aluminum coating (a few nanometers). The small thickness of the foil allows γ-particles from a Fe^{55} source to penetrate into the drift region. The cathode foil is also glued to a similar FR-4 frame. The GEM and the cathode frames fit on the PCB as shown in fig. 3.2(a).
The PCB rests on a thick aluminum base plate as show in fig. 3.2(b). The base plate has adapters for the gas inlet and outlet. The adapters are internally mapped to holes on the PCB to circulate gases through the chamber.
An aluminum frame (fig. 3.2(b)) covers the GEM-cathode assembly. The inside walls of the frame have a polyvinyl chloride (PVC) coating. The PVC material has good insulating properties and the coating prevents any HV discharges to the walls of the frame. The frame is wide enough that it does not touch the GEM-cathode assembly from the inside. The base of the frame is also made up of a thick Polystyrol layer, which insulates the frame from the PCB. A rubber gasket between the frame and the PCB makes the chamber leak-tight. On top of the frame, a transparent polyester window (thickness 50 μm) allows the γ-particles from the source to enter in the chamber.
The chamber and the pre-amplifiers are enclosed inside a steal box for proper shielding of the electronics (fig. 3.3).

[1] Mylar film, developed by DuPont.

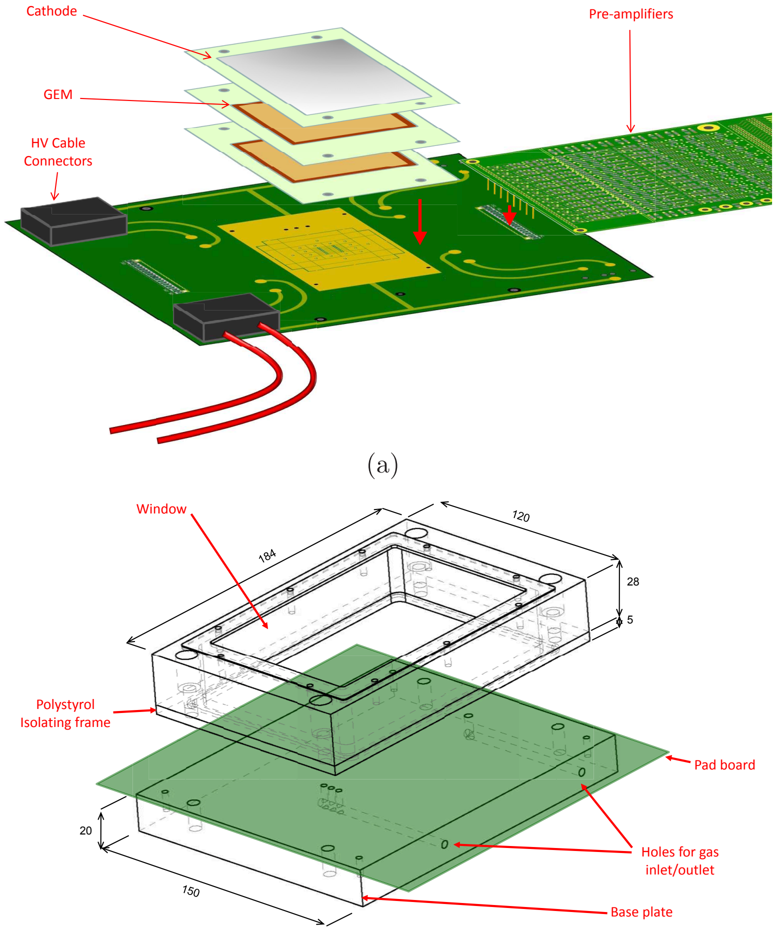

(a)

(b)

Figure 3.2: Test chamber's mechanical assembly: (a) a 3-D drawing of the PCB showing how the two GEMs, the cathode and the pre-amplifiers fit on it. The pads are located at the center of the PCB. Notice the connectors where the pre-amplifiers connect (one on the right side and another on the left side). The GEMs and the cathode HV connections (black boxes) are also on the PCB. (b) A drawing showing the chamber's covering frame and the base plate (all length units are in millimeters). There are two adapters on the base plate where the gas inlet/outlet lines fit. Notice the corresponding holes on the PCB shown in (a) [30]. Fig. D.1 in appendix D shows photographs of the test chamber assembly.

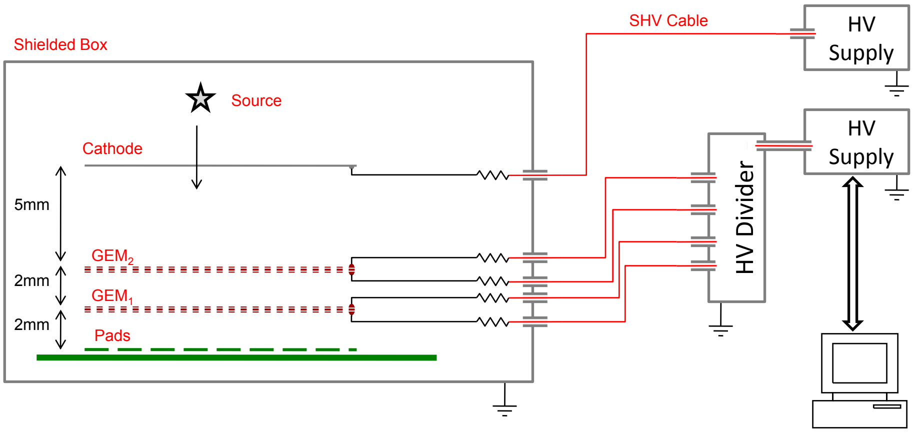

Figure 3.3: Test chamber schematic, showing the GEM-cathode arrangement above the pads and their connections with the HV system.

3.1.2 Pad Plane

The segmented pad plane is at the center of the PCB. There are 32 pads in total (as shown in fig. 3.4). These are connected to the readout electronics by means of two connectors having 16-pins each (see fig. 3.2(a)).
All the pads have a rectangular geometry. Their areas are, however, different: $34.1 \times 27.8\,\text{mm}^2$, $6.8 \times 4.9\,\text{mm}^2$, and $6.8 \times 1.1\,\text{mm}^2$. With this arrangement of pads, many different studies are possible. For a TPC with pad readout, a pad size smaller than the smallest size used here, would increase the complexity of the readout electronics, making it hard to implement. Hence, the smallest size was limited to $6.8 \times 1.1\,\text{mm}^2$. Only 7 out of these 32 pads are used for the measurements presented in this thesis. These are discussed in more detail in the next chapter.

3.2 The Time Projection Chamber

A TPC prototype is being built which will use a similar GEM-cathode assembly as the test chamber. Its pad plane, however, will have a different structure.
The TPC's field cage is a cylinder of length 500 mm. Its inner radius and thickness are 120 mm and 6 mm, respectively. Fig. 3.5 shows the field cage layout. Its main body is formed of a cylinder with two flat rings, one at each end, supported by angular brackets as shown. The two ends of the central cylinder are sealed by detachable lids. There are O-rings to ensure leak-tight sealing. One of the lids has an attached rectangular box that houses a HV cable connector. The same lid holds the cathode. The other lid holds the endcap assembly (not yet implemented). Each of the lids has two openings for the gas inlet and outlet.
The entire field cage body is formed of light weight materials like polyimide, poly-paraphenylene terephthalamide[2] and glass fibers [30]. Together, they form a very rigid and mechanically robust structure. The dielectric properties of the materials used, allow them to withstand high potential differences.

[2]Kevlar fibers, developed by DuPont.

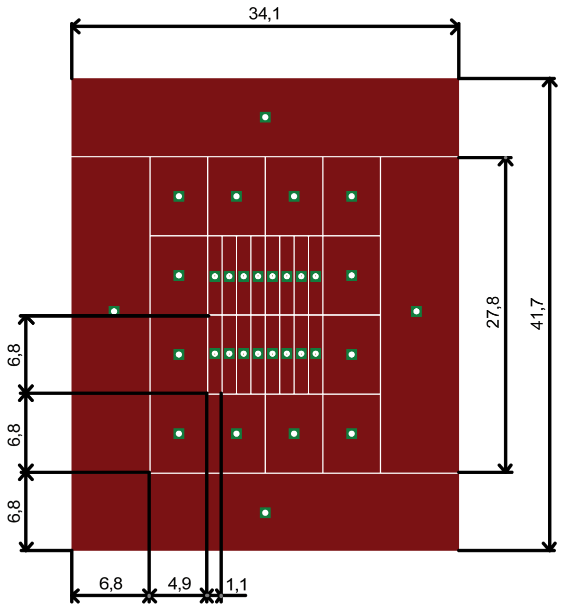

Figure 3.4: The figure shows a close-up of the pad plane. There are a total of 32 pads: 4 large sized ($34.1 \times 27.8\,\text{mm}^2$), 12 medium sized ($6.8 \times 4.9\,\text{mm}^2$), and 16 small sized ($6.8 \times 1.1\,\text{mm}^2$) pads [31].

The outer surface of the cylinder is conducting and is meant to be kept at ground potential, while the inner surface is formed of a flexible printed circuit with parallel strips of copper. These strips of copper are meant to provide a uniform drift field through the cylinder volume, by means of a potential divider network of resistors directly implemented on the printed circuit.
A more detailed discussion of the TPC's field cage is beyond the scope of this thesis.

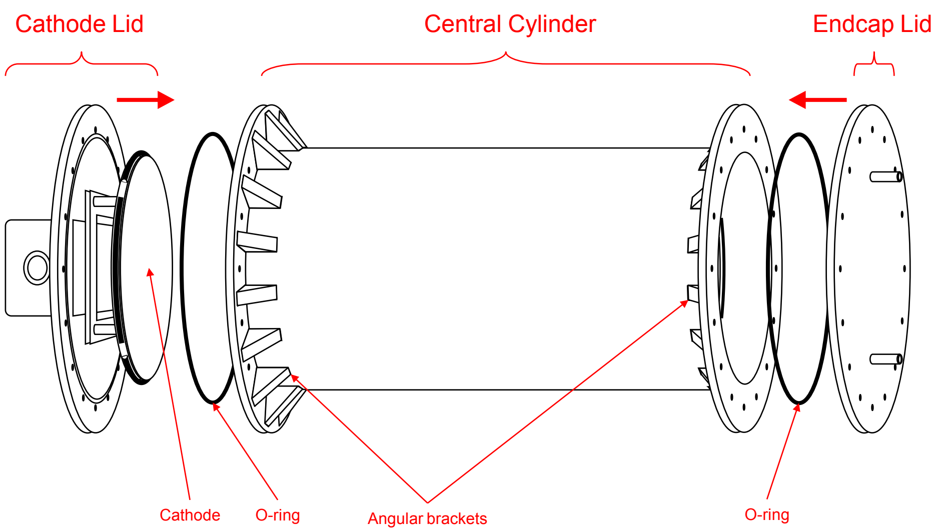

Figure 3.5: TPC's field cage assembly [30].

3.3 The Gas System

Careful selection and monitoring of gas quality is imperative for stable operation of gas detectors. The gas amplification varies with varying temperature, pressure and gas impurities. Presence of impurities like oxygen or moisture can affect the drifting electrons in the detector and consequently the detector's overall performance. Therefore, the gas system is designed to:

- be able to monitor the temperature and pressure of the gas;
- allow setting of quench gas fractions;
- be properly isolated from the atmosphere;
- be able to provide a moisture-free environment for the storage of the detectors while they are not in use;
- allow channeling of the gases through the desired detector (the test chamber or the TPC) whenever required.

3.3.1 Design and Layout

Fig. 3.6 shows a schematic diagram of the gas system. It features two main channels, one for the test chamber and the other for the TPC. There is also a third channel that includes a gas gain monitor (see section 3.3.3) which can be shared by the other two channels. Whenever required, the gas system can be configured, such that the gain monitor is either in front or behind a detector (pre- or post-mode respectively, fig. 3.7).
The gas system has three input lines:

1. A standard gas mixture for reference and calibration: an Ar-CO_2 mixture with 8 % CO_2 [3].
2. A custom gas mixture: an Ar-CO_2 mixture with variable CO_2 concentration. The mixer is not yet implemented. The gases will be mixed using electronically controlled mass flow meters.
3. A dry air supply for storing the detectors in a moisture-free environment when they are not in use.

Three glycerine-filled bubblers are employed at the gas exit points, i.e. each channel has its own dedicated bubbler. They let the exhaust gases out into the atmosphere as well as prevent contaminants, for example, oxygen and moisture, from entering the gas system. This technique works if there is a slight over pressure, in those channels, compared to the atmospheric pressure. The bubblers also help visualize if there is any gas flow through the detectors. The flow rate, however, can be measured by means of flow meters on those channels (except for the gain monitor channel).

[3]Commercially known as “ATAL-4”, AIR LIQUIDE Deutschland GmbH.

The amount of gas flow can be controlled by flow control valves on each channel. Control valves A and B are used, in combination with C, to divide the gas flow between their respective channels and the gain monitor (post-mode only). For example, the setting of A and C will decide what fraction of the gas coming out of the test chamber will flow through the gain monitor. Shunt valves D and E are used to disable, temporarily, the flow through the gain monitor, or to switch back to the former state without altering anything. In this way the settings of A (or B) and C can be preserved from one measurement to another.
Each channel also has, additionally, a pressure meter that shows the absolute pressure in that detector upto 1 bar. Their purpose is to show if the detectors are accidently subjected to harmful pressure levels.
The temperature of the gas is not easy to control due to poor insulation of the gas lines that connect the gas system to the detectors. The bubblers maintain the pressure in the system equal to the atmospheric pressure. Therefore, changes in the atmospheric temperature and pressure will affect the gas density in the detectors and hence the gas amplification, electron drift, etc.. This makes monitoring of atmospheric temperature and pressure changes very important to understand the behavior of the detectors. To meet this requirement a temperature and a pressure sensor were added to the setup. This is briefly described next.

3.3.2 Gas Temperature and Pressure Monitor

To be able to review temperature and pressure changes during and after an experiment, it is convenient to save these measurements digitally. Such a device is, essentially, a temperature and a pressure sensor connected to an analog-to-digital converter (ADC), read by a computer. A temperature and pressure monitor (TPMon) was built with an ADC card and an USB interface to a computer (fig. C.2 in appendix C shows the circuit diagram). The pressure sensor is mounted inside the TPMon device, while the temperature sensor is external (mounted at an end of a long metallic tube, to prevent any influence of the heat generated by the electronics). The device is placed at a convenient location in the laboratory.
To acquire data from the TPMon device, a Linux command-line utility was developed. The utility, called "`gas_tp_raw_data_demon`", constantly reads data from the device at a specified frequency and saves it into binary files along with the time stamp information. The data can be displayed as a function of time, using another utility called "`gas_tp_mon`". Fig. 3.8 shows a screen-shot of the TPMon applet. This is a ROOT application [32], which can be used in both online and offline modes, i.e. with or without the demon running. It divides the total data taking time period into smaller time intervals, say n intervals of size Δt. The time interval Δt can be specified in seconds. The program averages any data within this time interval before plotting it on the canvas. The number of averaged points would be $n' = \Delta t f_\mathrm{r}$, where f_r is the frequency at which the data is read from the device. In this way the variation of the data around its true value, due to quantization (a consequence of analog-to-digital conversion) and random noise, can be averaged during that time interval. The error-bars in fig. 3.8 show the computed root mean square (RMS)

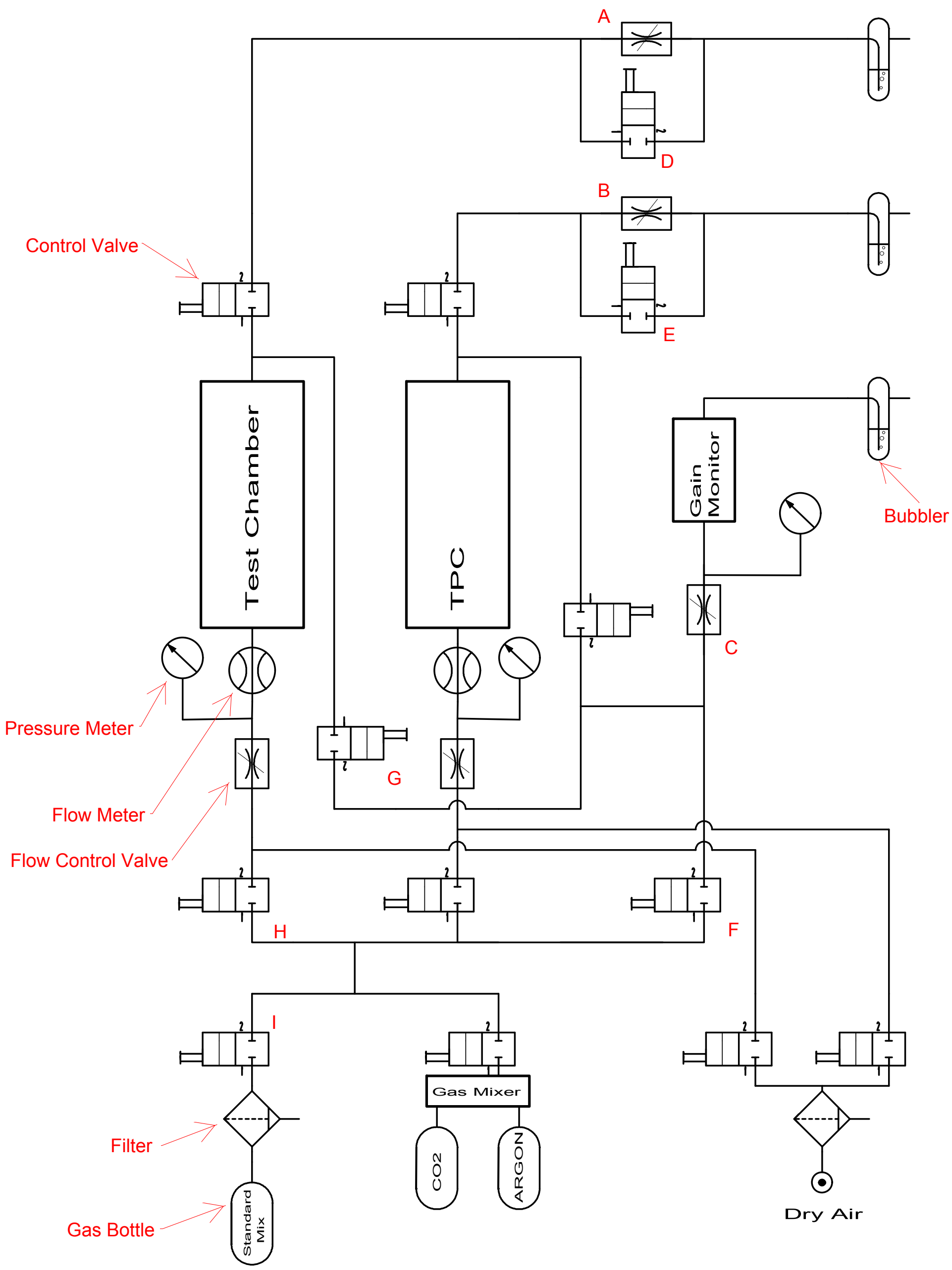

Figure 3.6: Gas system schematic: the symbols have their usual meanings; important ones have been labeled. All of the above, except the gas mixer, have been implemented [30]. Fig. D.2 in appendix D shows photographs of the gas system.

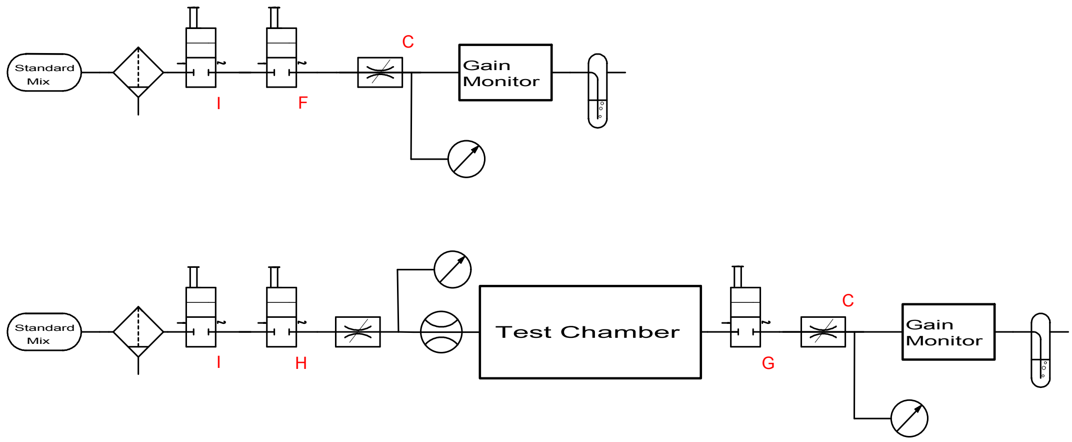

Figure 3.7: Gas system modes: the two circuits shown above are simplified versions of fig. 3.6 (the irrelevant channels are removed for simplicity). The first one describes the pre-mode, and the second one, the post-mode. The pre-mode is used to define a point of reference of the gas quality. In the post-mode, the gain monitor reports the gas quality, after the gas has traveled through the detector [30].

error during an interval. The TPMon applet complements the gain monitor: when both are run side-by-side, it is easy to check if the gain variations are due to changes in the ambient temperature and pressure, or due to the gas composition.

3.3.3 Gas Gain Monitor

The working principle of proportional counters was briefly discussed in section 2.4. The two peaks of Fe^{55} spectrum described therein have Gaussian distributions due to local gas gain variations. The center of these distributions corresponds to the average gas gain for a given gas density. An increase in the gas density decreases the average gas gain and consequently the peaks shift to the left in the spectra. The gain monitor (GMon) should show this effect.

Setup

A GMon device was developed, in-house [33], to monitor the gas gain variations with time. The device consists of a single wire proportional tube with a window to let ionizing particles in. The window is sealed with a copper foil thin enough (thickness $\sim 1\,\mu$m copper and $\sim 50\,\mu$m polyimide foil[4]) for this to work. The tube has an inner diameter of 12 mm (outer diameter 14 mm) and the wire's thickness is $30\,\mu$m. Its two ends are sealed with insulating plugs and it has only two openings for the gas inlet and outlet. The ionization is provided by means of a Fe^{55} source (see table C.2 in appendix C) placed close to the window. The source and the tube are packed within a lead casing (fig. 3.9(a)). The casing is grounded and therefore the tube as well.

[4]Kapton film, developed by DuPont.

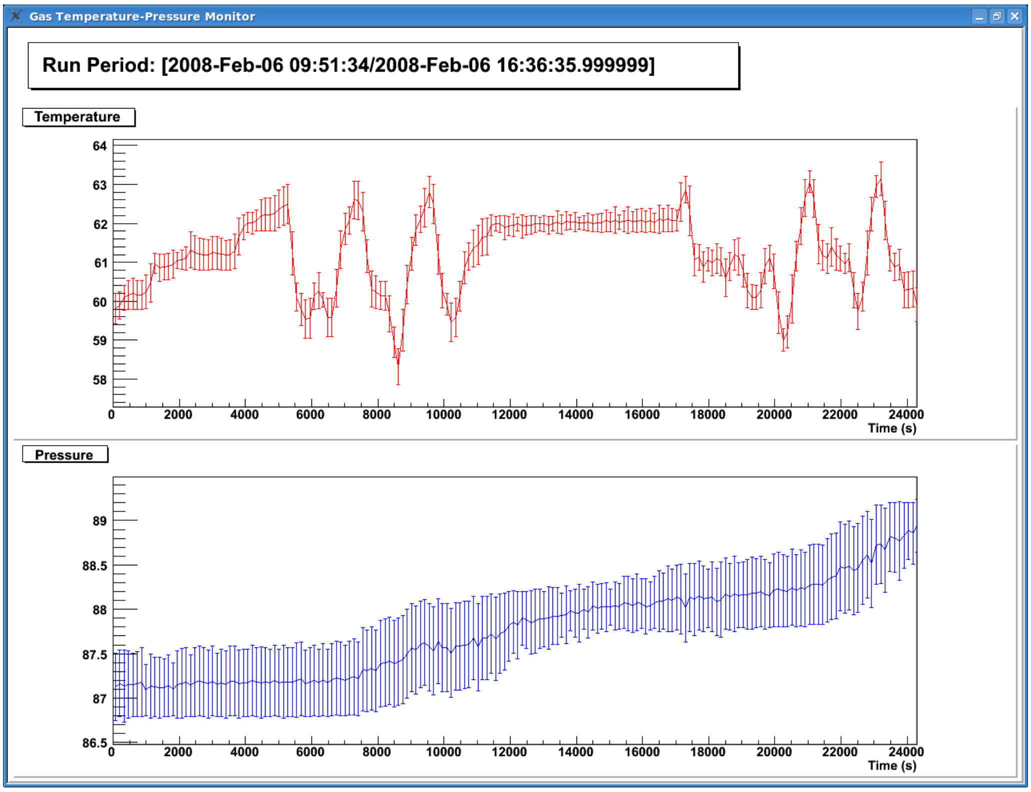

Figure 3.8: Screen-shot of the temperature and pressure monitor applet: "Run Period" reports the time period during which the demon was active. The y-axis values are in ADC units.

A schematic diagram of the GMon device setup is as shown in fig. 3.9(b). It consists of a pre-amplifier and signal shaper, a main amplifier, a HV power supply, and a multichannel analyzer (MCA).
The signals are decoupled through a capacitor C, passed through the pre-amplifier and shaped inside the device. The shaper is described in reference [34]. The device is installed behind the gas system and a LEMO cable connects the output of the shaper to the main amplifier. The main amplifier's gain is adjusted to make proper use of the MCA's range.

Software

The GMon software has two components. The first is a data acquisition (DAQ) application, which runs on a data station (a dedicated computer that reads the MCA device). It builds pulse height spectra of the signals received from the main amplifier. The spectra histograms are extracted from the DAQ application and stored as binary files on the data station. This task is performed by a script. The script monitors the spectrum region of interest (ROI), i.e. a pre-defined range of the spectrum, to generate a reset signal, when the ROI sum reaches a pre-defined value. The ROI sum is the sum of the bin contents within the ROI. The reset signal is used to starts a new measurement cycle automatically. In this way one data taking cycle follows another and a spectrum histogram file is generated every time. In the work

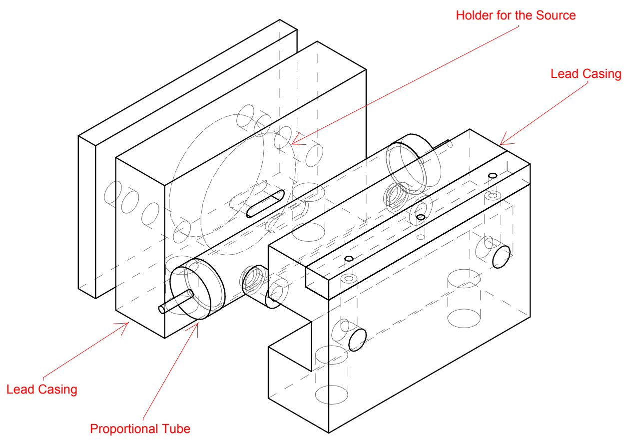

(a) Gain monitor proportional tube assembly [30].

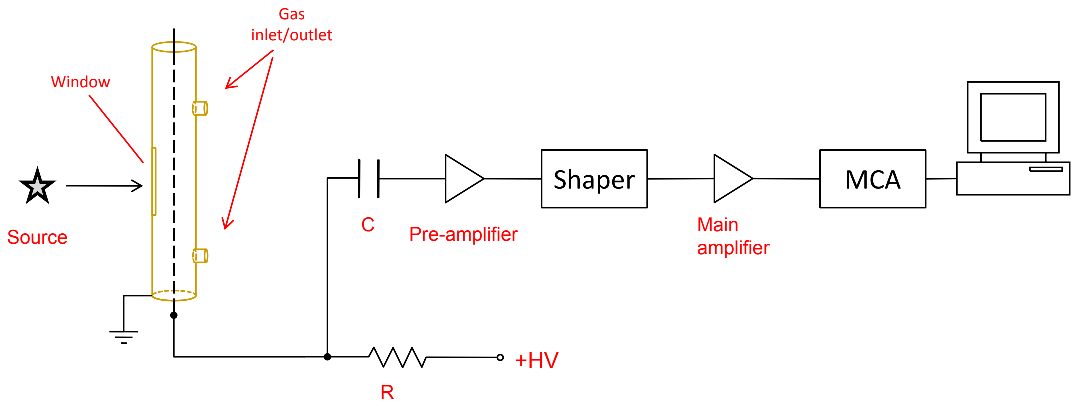

(b) Other components of the gain monitor.

Figure 3.9: Gain monitor hardware components: the tube, the pre-amplifier and the shaper are all installed inside a single box. The main amplifier and the HV supply modules are mounted inside a NIM crate. The MCA is installed inside a computer. Fig. D.3 in appendix D shows a photograph of these components.

presented here this value was chosen to be 50,000 counts, which corresponds to a counting time of $\sim 133\,\mathrm{s}$ using a 4 MBq source. This setting provides good statistics for the peak-search algorithm.

The above process generates a collection of spectrum histogram files. The next step is spectra analysis. This is done in two stages: finding peaks in individual spectra files; and showing the peak displacement as a function of time. These tasks are performed by a utility called "`gas_gain_mon`".

Fig. 3.10(a) shows the GMon applet display from an actual experiment (the lines are drawn only for demonstration and they are not a part of the display). It shows the displacement of the peaks, in units of the MCA channel number, with respect to time. The upper and the lower curves correspond to the Fe^{55} 5.96 keV peak and the Argon escape peak, respectively.

The peak-search algorithm used here is described in references [35, 36]. The algorithm, first, removes the continuous background from the spectrum and generates a smooth spectrum using the Markov chains method. For a specified standard devia-

tion ($\sigma = 50$) of the peaks, the algorithm then assumes a Gaussian response function which is used to obtain a deconvoluted spectrum (as shown by the smooth curves in figs. 3.10(b) and 3.10(c)). Then, the peaks falling below a specified threshold percentage of the highest peak amplitude are ignored. A threshold value of 2 % was used in the work presented here, to neglect the background peaks.
When the GMon device is switched from the pre-mode to the post-mode, the Ar-CO_2 mixture slowly replaces the dry air in the test chamber. As a consequence, the gain rises gradually (shown by the part of the graphs between the two vertical lines in fig. 3.10(a)) until it reaches a steady value comparable to the one prior to the switch (shown by the part of the graphs to the left of the dotted line in fig. 3.10(a)). The monitor rejects the spectra for which the peak-search algorithm returns a peak-count other than 2. For example, the spectrum shown in fig 3.10(b) has an unusual third peak at the far-left side. After the switch from the pre-mode to the post-mode, the acquisition application does not receive any signals within the ROI for a while, i.e. the ROI sum does not change during this interval. When the signals appear again, they have lower gains, and therefore, the new peaks start appearing on the left side of the ROI. Such peaks are not plotted on the applet display. For comparison, see fig. 3.10(c). Notice the difference between their counting times ("Duration"). Fig. 3.10(b) shows a spectrum after the gain has already stabilized.

3.3.4 Gas System Operation

The gas system is always set to flow dry-air through the detectors when not in use. An experiment with the detectors first starts with proper initialization of the gas system. The following procedure is always exercised:

- First of all, the dry-air flow through the detector is turned off.
- The TPMon device is turned on and the corresponding software utilities ("`gas_tp_raw_data_demon`" and "`gas_tp_mon`") are initialized.
- The GMon device is switched to (if not already in) pre-mode (as shown in fig. 3.7) and the standard gas mixture is passed through it. In this mode the GMon applet would display the gas gain in the pure gas mixture.
- The power and high voltage of the GMon device are switched on.
- The DAQ application is initialized along with the GMon applet ("`gas_gain_mon`").
- After the peak displacement curves saturate, i.e. the gain does not vary anymore, the GMon device is switched to the post-mode. In this mode the GMon applet would display the gain of the exhaust gas from the detector. The peaks momentarily disappear and slowly return back to their former position as the detector is flushed completely.
- After the peaks return to their former positions, further experimental tasks may be performed (e.g. turning the detector high voltage supplies on).

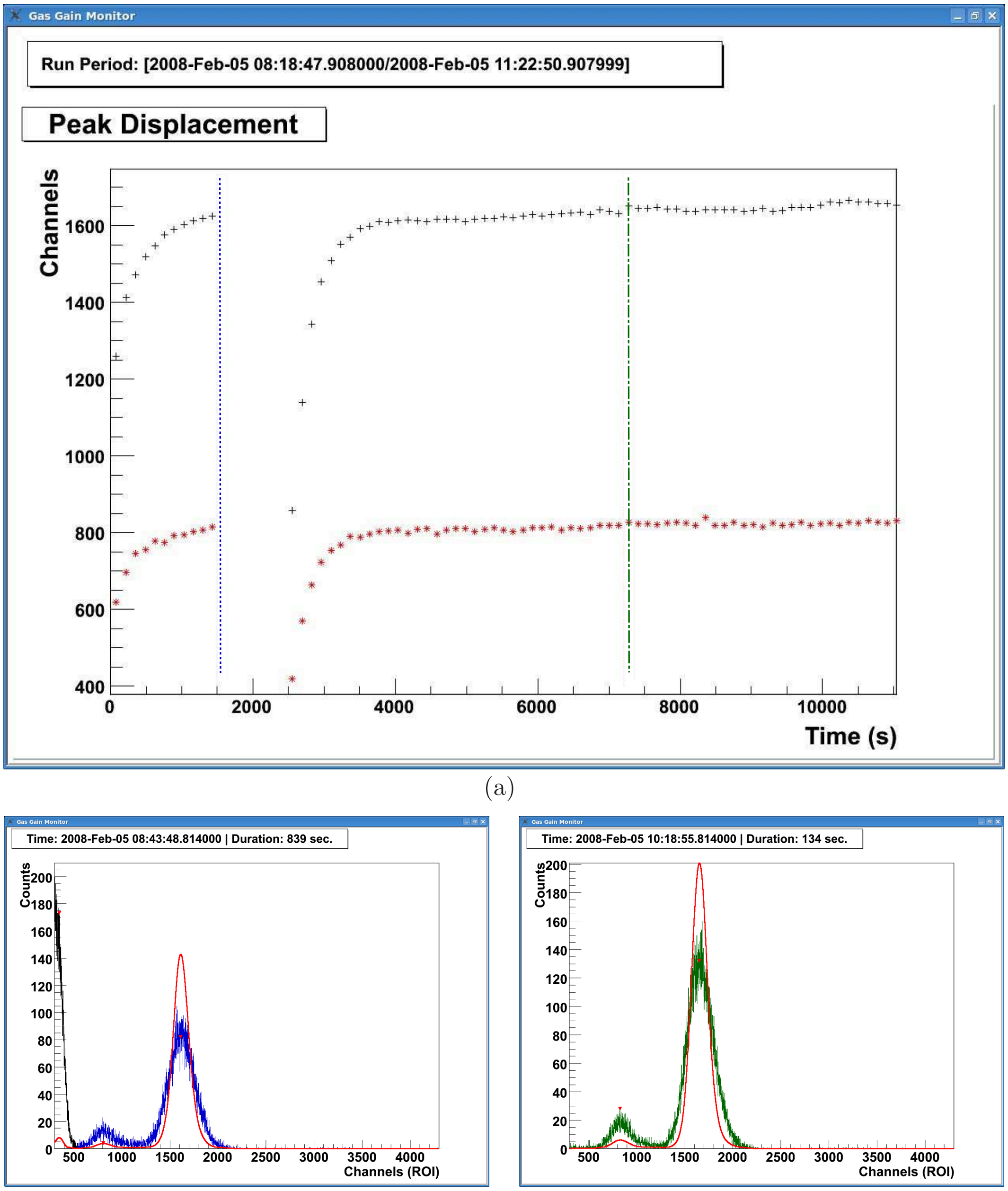

(a)

(b) (c)

Figure 3.10: Screen-shots of the gas gain monitor applet: these are the results of a gain monitoring session during an actual experiment. (a) shows the peak displacement curves: the upper and the lower curves correspond to the Fe^{55} 5.96 keV peak and the Argon escape peak, respectively. The monitor was switched from pre-mode to post-mode after about 1500 s. The effect on the gas gain of Ar-CO_2 slowly replacing the dry-air in the test chamber is clearly visible. (b) Is an example of a spectrum (3 peaks) which was rejected by the monitor (immediately after the switch over). The corresponding points do not show up on the monitor display (the dotted line in (a)). (c) shows how a normal spectrum looks like. There are exactly 2 peaks. This is the spectrum corresponding to the points in (a) marked by the dash-dotted line.

3.4 The High-Voltage System

The detectors need high voltage (HV) supplies for the following purposes:

- To set the drift cathode voltage to provide a drift field in the detector.
- To set the cathode and the anode voltages of each GEM in use, to get the desired gas amplification.

One HV supply module can be used for everything, if its output voltage is high enough. Then, a resistive divider network can be used in a way that it provides the right voltages on each of these devices for their proper functioning. However, the HV divider method cannot be used for studies that require these voltages to be variable parameters. Moreover, it is difficult to determine in this case the optimal voltages giving the best results.
Hence, early experiments were performed with five different HV supply modules: one for the cathode and two for each of the two GEMs. Although quite flexible, this approach has drawbacks [25]. The outputs of different HV supplies vary with respect to each other. Hence, a temporary increase in the GEM voltages, due to different voltage sources, could lead to sparking and permanent damages in GEMs. Reference [25] describes the various HV supply schemes that can be used as an alternative.
The present HV system uses two HV supply modules to provide voltages to the test chamber electrodes. The first module (refer to table C.1 in appendix C for specifications) is used for the drift cathode alone. The other module is used with an external HV divider network as shown in fig. C.3 (appendix C), to provide voltages to the two GEMs. Both the modules have a ramp-up setting of 2 V/s. However, the second module has a serial RS-232 interface that allows the module's monitoring and control using a computer. This has not been implemented for the drift cathode HV supply module yet. An applet[5] monitors how stable the divider voltage actually is. The applet also allows a custom control of the ramp-up process. The HV is delivered to the corresponding test chamber electrodes by means of SHV cables (fig. 3.2(a)).

3.4.1 High-Voltage System Operation

To prevent any accidental HV changes, that can damage the GEMs, it is important to automate the ramping and avoid, as much as possible, any manual adjustment of the HV modules' potentiometers. The GEM voltage ramping is controlled by a computer. However, the drift cathode HV supply is set to ramp-up, automatically, to a maximum value of 2200 V, when turned on. Both the ramp-ups are triggered simultaneously.

[5]Designed using LabVIEW from National Instruments [37].

3.5 The DAQ System

The various components of the DAQ system are shown in fig. 3.11. The DAQ system digitizes the signals from the pre-amplifiers and stores them on a data station so that they can be analyzed later. The digitization process is triggered on one of the signals from the pre-amplifier. The following few sections describe the DAQ system setup in detail.

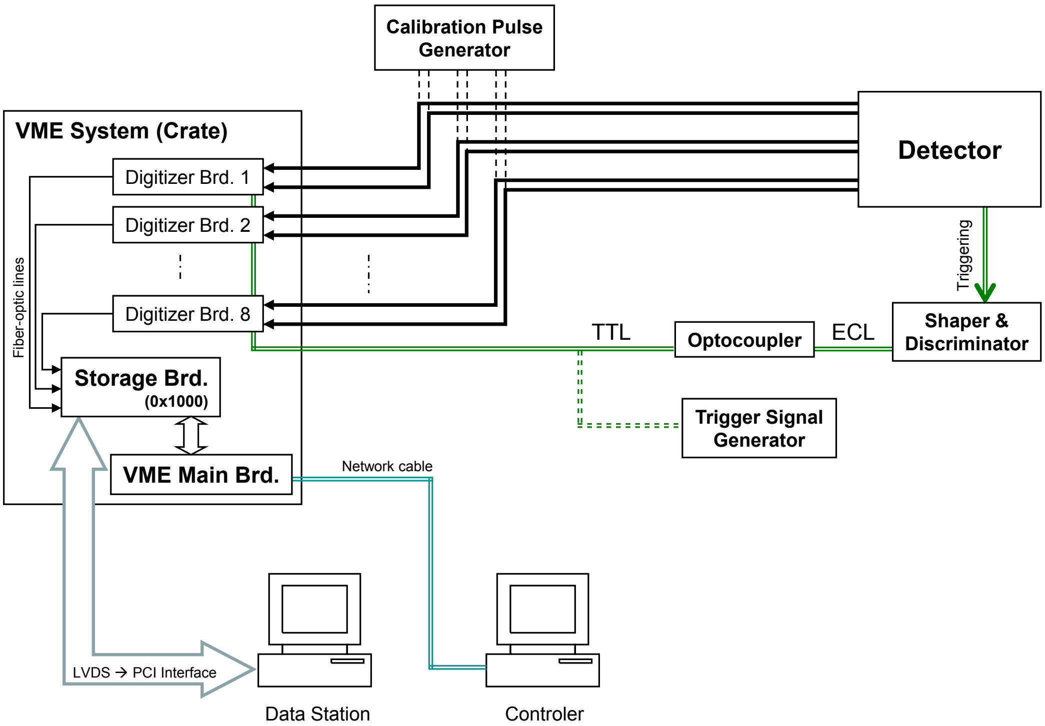

Figure 3.11: There are four main components of the DAQ system: the digitizer boards; the storage board; the data station; and the trigger electronics. Each digitizer board has two channels, where signals from the detector's pre-amplifiers can be fed in. The digitized data packets are sent to a DAQ terminal (data station) via the storage board. The data station is a computer with a PCI-LVDS interface to the storage board. The VME system is initialized and checked by the control computer. The trigger signals are obtained from a chosen pre-amplifier output.

3.5.1 Setup

The foremost components of the DAQ system are the digitizer boards. A maximum of eight digitizer boards can be installed in a single VME crate. Each board has two channels for signal input, a trigger input and an event counter reset input.
One or both of the input channels, of a digitizer board, can be used if required. If only one channel is used, the other channel is terminated with a $50\,\Omega$ resistor. The signals to be digitized, must have negative amplitudes ranging from $-50\,\mathrm{mV}$ to $-1000\,\mathrm{mV}$.

A positive transistor-transistor logic (TTL) signal at the trigger input triggers a measurement cycle. It also increments a 32-bit event counter and initiates the data transmission process.
The digitization is performed by two sets of four time interleaved FADCs (flash ADC), one set for each channel. The FADCs have a 12-bit resolution and they operate at a frequency of 62.5 MHz. Hence, the total achievable sampling rate is $4 \times 62.5\,\text{MHz} = 250\,\text{MHz}$ (sampling period 4 ns). A time resolution of 4 ns allows precise rise time and fall time measurements of the signals. The digitization process runs for 378 clock cycles in a sequence. Thus, a measurement cycle lasts $378 \times 16\,\text{ns} = 6048\,\text{ns}$ (since the clock frequency is 62.5 MHz). The outputs of the FADCs are first stored in first-in first-out (FIFO) memories before transmitted.
The data transmission starts as soon as there is some data available in the FIFOs. The state machine is implemented in a field-programmable gate array (FPGA). The FPGA logic builds data packets and transmits them to a, so called, storage board through a fiber-optic link (with a transmission frequency of 40 MHz). Fig. 3.12(a) shows simulated[6] transmission timings of the data packets. A packet contains 1036 Bytes. It carries headers and data from all the eight FIFOs. The entire data set is transmitted in six packets. During data transmission, parity and cyclic redundancy check (CRC) information, along with event and packet identification information are appended to each packet. Fig. 3.12(b) shows a close-up of the first packet's transmission process. The 6 μs long pulses, labeled "FIFO∗_~WEN", enable the writing of the FADC data to the FIFOs. Notice the comparator signal that triggers the process. When the FIFOs have some data the "FIFO∗_~REN" (FIFO read enable) pulses enable transmission of the FIFO data one-by-one.
The measurement time is only 6 % of the total transmission time (as can be seen in fig. 3.12(a)). The reason is simple: the data is serialized in order to transmit it through a single channel. Hence, the transmission time ($\sim 100\,\mu$s) determines the dead-time of the DAQ system. The dead-time is insignificant if the trigger rate is less than 10 kHz, for example, in case of cosmic particles.
The data storage board collects the data packets from all the eight digitizer boards. It buffers the data in eight corresponding channel FIFOs, and sends it to the data station via a LVDS interface. For this to work, the VME[7] system has to be properly initialized. A control station is used to logon to the VME system (network interface) and to execute programs there. These programs not only initialize the system, but also allow its debugging and status checking.
The data station contains a PCI card, that receives data from the digitizer board via the LVDS link. The card, the digitizer and the storage boards, were developed in-house (originally published in references [38, 39]).

Trigger Setup

The TPC will use a scintillator hodoscope with photomultipliers to trigger the state machine. The test chamber, however, uses a "self-triggering" method. Depending on

[6]Simulated with Quartus II simulation software.
[7]Versa Module Europa (VME), IEEE standard.

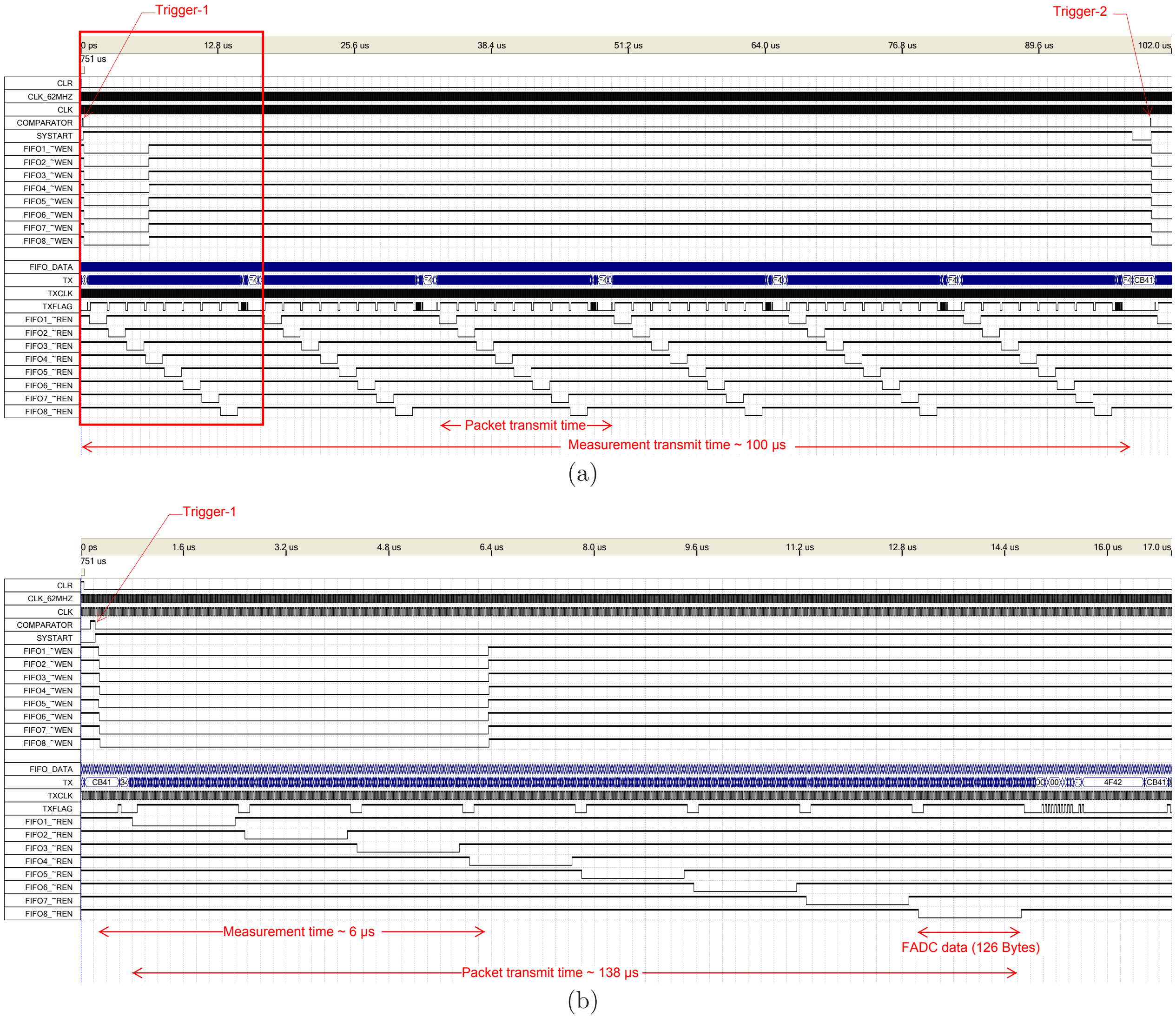

Figure 3.12: Packet transmission timings: (a) total transmission time. (b) An enlarged part of (a) as shown [40].

the experiment, a suitable pre-amplifier channel is used to obtain a trigger signal. Every pre-amplifier channel has a positive and a negative output. The negative outputs are required for the digitizer boards. Hence, the positive outputs are used to produce the trigger signal.
A discriminator selects signal amplitudes for generating the trigger signal. The discriminator is a NIM module (described in reference [34]), that provides an emitter-coupled logic (ECL) output. The discriminator and the trigger inputs of the digitizer boards are connected via an optocoupler to avoid ground loops. The optocoupler includes the necessary ECL/TTL conversion electronics.
Although only short LEMO cables were used to connect the various devices described above, the trigger signal was delayed due to the trigger electronics by more than 100 ns. Hence, all signal channels had to be delayed using long BNC cables to compensate for this delay. This, however, will not be necessary in case of the TPC, where the trigger signal will arrive much earlier than the chamber signals (at the pre-amplifier outputs).

3.5.2 Software

The following few sections describe the most important software components of the DAQ system, starting with the data packet, which was introduced earlier.

The FADC Data Packet

The structure of a data packet is as shown in table 3.1. A 32-bit pattern marks the beginning of the packet (hexadecimal "`0xd347cb41`"), called the "magic words". They are used to identify a packet in a stream of data. A similar purpose is served by the "end-of-block word" (hexadecimal "`0x4f42`"). Together, they enclose 1030 Bytes (or 515 Words) of data.
The first 1008 Bytes (of the 1030 Bytes) contain the data from the eight FADCs and the rest describes the data packet itself. The digitizer board ID, identifies the source of the packet, i.e. the digitizer board where it originated. The data from one measurement is transmitted in six packets. The packets are identified by their packet IDs. Likewise, the event number is given by the Event ID. The parity and the two CRC words can be used to check the integrity of the data contained in the packet.

PCI Driver and Data Stream

The PCI interface is handled by a Linux device driver [39] on the data station. Once the VME system and the driver, are properly initialized, the driver writes the data available on the PCI device, to a 128 MB ring-buffer in the main memory of the data station. The ring-buffer is a memory area, the driver shares with user processes. The data in the ring-buffer is volatile, i.e. it will be overwritten by the driver as soon as it completes a write cycle. It is the responsibility of the user process to save the data while it is available in the buffer [41].
A C++ library was developed to retrieve and save the data from the buffer to the

Data Item Description	**Data Type**	**Size**
Magic words (`0xd347cb41`)	unsigned integer	32-bit
Channel-A data		
FADC-1 data	unsigned integer array	63×16-bit
FADC-2 data	unsigned integer array	63×16-bit
FADC-3 data	unsigned integer array	63×16-bit
FADC-4 data	unsigned integer array	63×16-bit
Channel-B data		
FADC-1 data	unsigned integer array	63×16-bit
FADC-2 data	unsigned integer array	63×16-bit
FADC-3 data	unsigned integer array	63×16-bit
FADC-4 data	unsigned integer array	63×16-bit
Digitizer board ID	unsigned integer	16-bit
Packet ID	unsigned integer	16-bit
(unused)	unsigned integer	64-bit
Event ID	unsigned integer	32-bit
CRC-1	unsigned integer	16-bit
CRC-2	unsigned integer	16-bit
Parity	unsigned integer	16-bit
End-of-block word (`0x4f42`)	unsigned integer	16-bit

Table 3.1: Structure of a FADC data packet: a data packet is 1036 Bytes long. The "magic words" form the packet header and can be used to identify packets in a continuous stream of data. The table lists the items, in the order they are arranged in the packet [40].

data station's storage media. The library is called "`liblctpc_readout_sys.so`". It offers two classes "`LCTPCDataSource`" and "`LCTPCRawData`" for retrieving and saving data packets, respectively. The former represents the data source, i.e. the ring-buffer, and maintains the status of the stream. When instantiated, the class resets the PCI device and claims a pointer to the ring-buffer. Thereafter, it returns data packets to the calling process, one-by-one, when requested. It also reports the "health status" of the packets being read from the buffer: a situation may arise, when the reading process (the user) is slower than the writing process (the driver) and the later overtakes the former, a part of the data packet may be lost. The health status report tells the calling process if a packet is valid or not.

Event Building and Storage

Some of the data packets transmitted by the digitizer boards are rejected by the storage board due to improper transmission. Although less probable, there could also be losses in sending the data from the storage board to the PCI card and at the retrieval stage discussed above. Hence, some packets have to be rejected at the time the data is being stored. This is done by the command-line utility called "`raw_data_demon`". It reads packets from the ring-buffer, checks their health status, and saves them if all test results are positive.

The transmission of the digitized data from the digitizer boards vary in speed from board to board. As a result, the data packets corresponding to an event are received at different times. The class "LCTPCRawData" manages the raw data storage for the demon. It organizes the packets in binary event files as and when they arrive.

Checking System Integrity

Apart from the basic functionality of the class "LCTPCDataSource", it provides other information, that can be interpreted to provide status reports of the DAQ system. There are two command-line utilities for status monitoring: "data_source_mon", and "event_mon".
The utility "data_source_mon" monitors the data source, i.e. the ring-buffer (or the driver). It reports, for each ring buffer cycle:

- any buffer overflows:
  - Problem: an overflow flag is set when the buffer writing process overtakes the reading process (described above).
  - Causes: slow system speed or system resources unavailable.
  - Effects: partial or complete loss of data. In either case, the data packet is rejected.
- skipped bytes (or data words):
  - Problem: (A) when a data packet has an unusual size. (B) Neither magic, nor end-of-block words, found.
  - Causes: (A) unavailable data for a long time due to: no trigger signal or improper connections elsewhere. (B) Data corruption during transmission.
  - Effects: irrecoverable data packet content. The data packet is rejected.
- bad packet headers:
  - Problem: either the magic words or the end-of-block word missing. If at least one of the magic or the end-of-block words is in place, the position of the data within the packet can be determined.
  - Causes: data corruption during transmission.
  - Effects: although the data could still be intact, its position within the packet may get wrongly estimated. The data packet is rejected anyway.

The CRC and parity checks have not been implemented yet.
The utility "event_mon" checks how complete the events are. In other words, this is a measure of rejection percentage. For example, if the rejection percentage is more than 50 %, it may not be time efficient to collect data on such a system.

3.5.3 DAQ System Operation

The following procedure is performed to use the DAQ system:

- First, the VME system is initialized as described earlier. The only setting important here is the correct specification of the storage board address on the VME bus. At present, this is simply "`0x1000`" (hexadecimal).

- Calibration run[8]: The FADCs need to be inter-calibrated to reduce digitization artifacts (described in the next chapter). A calibration pulse generator and a trigger pulse generator are connected instead of the signal and the trigger cables, as indicated in fig. 3.11.

  - The utility "`raw_data_demon`" is launched to get a certain number of calibration events. The process is terminated after enough data is collected.

- Measurement run: The generators are removed and the actual signal and trigger cables are replaced.

  - The utility "`raw_data_demon`" is launched again for collecting events from the detector. The process is terminated after enough data is collected.

- Calibration run is repeated.

[8]The calibration runs must be performed immediately before and after the measurement runs, for better inter-calibration of the FADCs.

Chapter 4

Signal Reconstruction

This chapter discusses the reconstruction of the signals from the test chamber using the DAQ system. Some measurements were performed to understand the shape of the signals, and to obtain estimates of the amount of signal sharing between adjacent pads. The first few sections describe the digitization process in more detail. The later sections discuss the results of the measurements, and any conclusion that can be derived from them.

4.1 Effects of Digitization

Chapter 3 discussed, briefly, the various components of the DAQ system. The digitization is achieved by means of four time interleaved FADCs. This section presents a closer view of the digitization process and its inherent problems.

4.1.1 Digitization Process in a Single FADC

A standard N-bit FADC has $2^N - 1$ comparators, that compare a source signal voltage with as many reference voltages as there are comparators. The reference voltages are obtained from a voltage divider network of equal resistances, as shown in fig. 4.1(a). The outputs of the comparators are encoded to obtain an N-bit number, that represents the source signal voltage level (at a given instant of time).
To understand digitization from a theoretical perspective, it is convenient to break it down into two stages: sample-and-hold (S&H) and quantization (Q). The sample-and-hold stage preserves the instantaneous value of the input signal during a sampling instant, while the quantization is the process of the conversion of this instantaneous value to the nearest integer. Both processes lead to the conversion of a continuous quantity into a discrete one, i.e. sample-and-hold converts the time variable from continuous to discrete and quantization does the same to the voltage. Both of them affect the quality of the digitized output. For example, if the input signal has frequency components above one-half of the sampling rate (Nyquist rate), those signal components will be “aliased” to frequencies below the Nyquist rate (see, e.g., reference [42]). This leads to loss of signal information and is also true for interleaved FADC systems. It imposes an upper frequency limit on the input spectra,

i.e. if the DAQ system has a maximum sampling rate of 250 MHz, the input signal must have a frequency less than 125 MHz, else the signal cannot be reconstructed correctly. In the work presented here, the maximum observed signal rate was less than 400 kHz, and the signal length was larger than 5 μs (much larger in comparison with the sampling instant of 4 ns). Hence, the signal shape information can be retained during the conversion process.
The other important phenomenon, that affects the signal quality, is the process of quantization. This involves conversion of a voltage level to the nearest integer value. The error introduced due to quantization is, at the most, $\pm\frac{1}{2}$ LSB (least significant bit). The effect of the quantization error is like addition of uniformly distributed random noise to the input signals. It has a standard deviation of $\frac{1}{\sqrt{12}}$ LSB ≈ 0.289 LSB. As mentioned in chapter 3, the FADCs used in the present setup have 12-bit resolution, the RMS noise added to the input signals due to quantization is then $0.289/2^{12}$ ($< 0.01\,\%$). In an interleaved FADC system, this error is insignificant compared to others (discussed next). Hence, it is ignored.

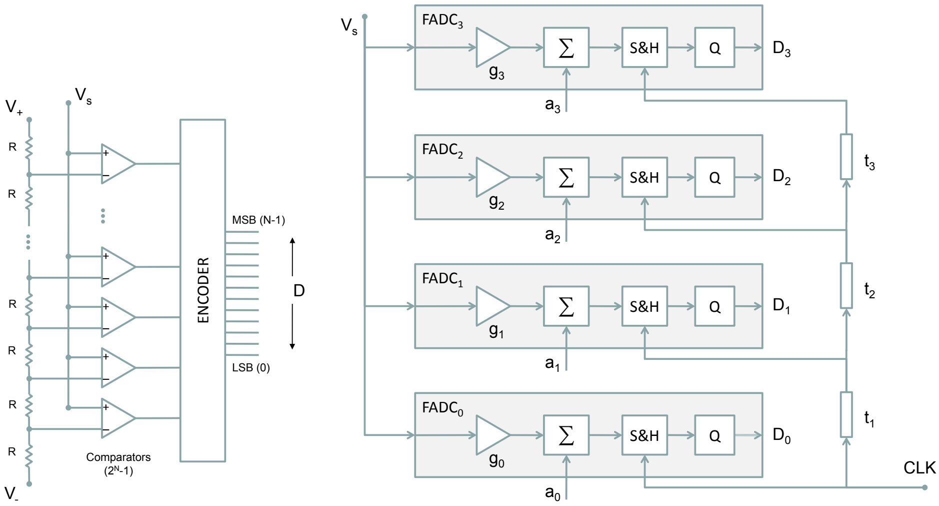

(a) (b)

Figure 4.1: FADC block diagrams: (a) shows basic components of a FADC. V_s represents the source signal and D is the digitized output. (b) shows a block diagram of a time interleaved FADC system. The FADC model shown here is described in reference [43]. t_1 through t_3 are time delays of 4 ns each. g_i and a_i are the gain and the amplitude offset errors of the i^{th} FADC. The FADC model assumes a sample-and-hold (S&H) stage before a quantizer (Q) converts an analog voltage level to an integer.

4.1.2 Digitization Process in Time Interleaved FADCs

Fig. 4.1(b) shows a block diagram of four time interleaved FADCs. t_1 through t_3 are time delays. They delay the clock pulse (62.5 MHz) by 4 ns each, to provide an effective sampling frequency of 250 MHz. The source signal V_s is applied to all the FADC channels and the digitized data appear at the outputs D_0 through D_3.
The FADCs have varying characteristics due to their fabrication process. Their gains

(g_i) and amplitude offsets (a_i) differ from each other and there are time jitter errors due to non-uniform clock delays. The digitized signals obtained from such a system have distortions owing to these systematic errors. For example, fig. 4.2(a) shows a raw, uncalibrated signal, reconstructed from the outputs of the four interleaved FADCs. Its noise has a standard deviation of about 17 LSB. In contrast, fig. 4.2(b) shows the output of a single FADC channel. The noise of the corresponding analog signal had a standard deviation of about 0.8 mV $\simeq$ 3.4 LSB, which is comparable with that of the reconstructed signal shown in fig. 4.2(b). Clearly, the other three FADC outputs have an offset w.r.t. this one that distorts their combined signal. Hence, knowledge of the gain and the offset errors of the FADCs, is important in order to minimize these distortions.

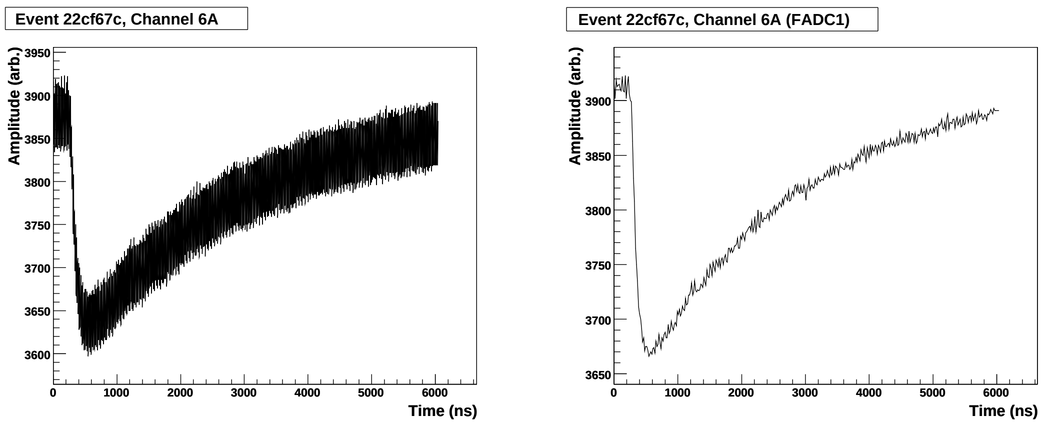

(a) (b)

Figure 4.2: Effects of the amplitude offset and the gain errors on the digitized output (the y-axis values are in FADC units): (a) A raw, uncalibrated signal (noise $\sigma \sim 17$), as received from the digitizers. (b) shows the FADC$_1$'s component for the sake of comparison (noise $\sigma \sim 4$).

4.2 FADC Data Inter-calibration

The estimation of the gain and the offset errors of the individual FADCs is not that straight forward and it is often based on sophisticated techniques which are rather difficult to implement. In the work presented here, a simple method was used to inter-calibrate the FADC data to minimize the distortion levels.
The method assumes the following to be true.

- The offset and the gain errors of the individual FADCs do not vary too much w.r.t. each other during a measurement run, i.e. effects of these errors are assumed to be constant in time.

- For individual FADCs, the effects of quantization can be ignored (as inferred in section 4.1).

- For individual FADCs, the random noise is normally distributed around their reconstructed signal. This, however, is not true if the analog signal noise is comparable with that introduced due to quantization.

The method uses a calibration signal, whose amplitude varies linearly with time, to obtain four datasets from the four FADCs. Since the generated analog wavefunction is linear, each dataset shows a linear behavior (with normally distributed random noise around it). Hence, the datasets can be compared and corrected. The objective of this method is to determine relative calibration functions that can be applied to the component datasets of a signal (of any sort), in order to minimize the distortion levels.
The calibration functions are obtained as follows:

- First, a triangular waveform is fed into the system at the input V_s. The parameters of the waveform are chosen, such that the amplitude spans the whole FADC range and its rise time is just as long as a measurement cycle ($\sim 6\,\mu$s). Thus, the resulting reconstructed waveform is just one line running from the lower-left corner to the upper-right corner of the amplitude vs. time graph, as shown in fig. 4.3(a).

- The outputs (D_i) of the four FADCs are stored in four data arrays, and one of them is chosen (arbitrarily) as the reference set. The reference set is plotted on an amplitude vs. time graph and a line is fitted through the most linear region of the graph (i.e. the entire graph, if it is linear).
  The reference line is assumed to be the true mean of the calibration waveform and the other datasets are corrected accordingly.

- Then, one of the other three arrays is selected. The relative offsets of each of its data points w.r.t. the reference line is plotted on a graph as function of its amplitude. The x-axis of the graph represents the reference line itself (zero offset). A line is fitted through the graph (see fig. 4.3(b)). The equation of this line is the calibration function for the FADC it represents. Notice that the line may not necessarily be parallel to the reference line. An important observation, however, is that the data points are Gaussian distributed with the line as its mean. This is also shown in fig. 4.3(b) by means of histograms.

- The procedure is repeated for the remaining two data arrays.

A flowchart of the above process is shown in fig. 4.4. Let $y_i[k]$ be the data array of k integers, carrying the i^{th} FADC's waveform amplitudes ($i = 0, 1, 2, 3$), and let $t_i[k]$ be the corresponding sampling times. Let the first dataset be the reference set. Hence:

$$y_{\text{ref}}[k] = y_0[k],$$
$$t_{\text{ref}}[k] = t_0[k],$$

are arrays containing coordinates of points on an amplitude vs. time graph (fig. 4.3(a)). Fitting a line through these points gives the equation of the reference line,

$y_{\text{ref}}(t)$. To obtain an offset $\delta_1[k]$, of the k^{th} point of the second dataset, its amplitude $y_1[k]$ is subtracted from the corresponding point on the reference line, i.e. $y_{\text{ref}}(t_1[k])$:

$$\delta_1[k] = y_{\text{ref}}(t_1[k]) - y_1[k]. \tag{4.1}$$

In this way, $\delta_1[k]$ can be computed for all values of k and plotted as a function of $y_{\text{ref}}(t_1[k])$ on a graph (fig. 4.3(b)). A linear fit through this graph, gives the calibration function for the second FADC ($i = 1$). If $\delta_i(y)$ is the calibration function of the i^{th} FADC, then their datasets are corrected using the following relation:

$$y_i^{'}[k] = y_i[k] + \delta_i\left(y_{\text{ref}}(t_i[k])\right), \tag{4.2}$$

where $y_i[k]$ and $y_i^{'}[k]$ are the original and the corrected datasets, respectively.
The four calibration functions for channel 6A were determined to be:

$$\begin{aligned}
&\delta_0 = 0,\\
&\delta_1 = 2.183 \cdot 10^{-02} \cdot y_{\text{ref}}(t_1[k]) - 9.853,\\
&\delta_2 = 4.846 \cdot 10^{-03} \cdot y_{\text{ref}}(t_2[k]) - 33.15,\\
&\delta_3 = 4.444 \cdot 10^{-03} \cdot y_{\text{ref}}(t_3[k]) - 8.358,
\end{aligned}$$

The above calibration functions were used to correct the calibration waveform itself (see fig. 4.5(b)), in order to check the quality of the calibration. Compare the histogram of the original waveform in fig. 4.5(a) to the corrected one in fig. 4.5(b). The effect of this is like merging the centers of the Gaussians of all the datasets, described above, into one.
Similarly, the method can be used to determine the calibration functions for each digitizer channel (in the work presented here, calibration was only necessary for channel 6A). These can be directly applied to correct signal distortions, an example of which is shown in fig. 4.5(c). In comparison with the same, but uncalibrated signal shown in fig. 4.2(a), there is a reduction of about 40 % in the signal noise. However, the resulting signal still has periodic noise components (not visible) owing to the mismatch errors in the FADCs, while the calibration pulse (shown in fig. 4.5(b)) itself is almost distortion free. This indicates that there are time dependent effects that the method does not incorporate (contrary to the first assumption of the method). See appendix B for a case study.

4.3 Signal Measurements

An experiment was performed to collect data for rise time and fall time measurements of the signals from the test chamber. The data was collected for three different pad sizes. Fig. 4.6 shows the pad numbering scheme used.
The event information was extracted from the datasets and the necessary calibration was performed as discussed above. For example, the first 20 events from a dataset are shown in fig. 4.7. Signals too small in amplitude are noisy and they are unfit for analysis. In order to select good signals from the dataset, only those with peaks lower than a threshold level (3750 arb. units) were selected (see fig. 4.7). The signal time measurements were performed in the following way:

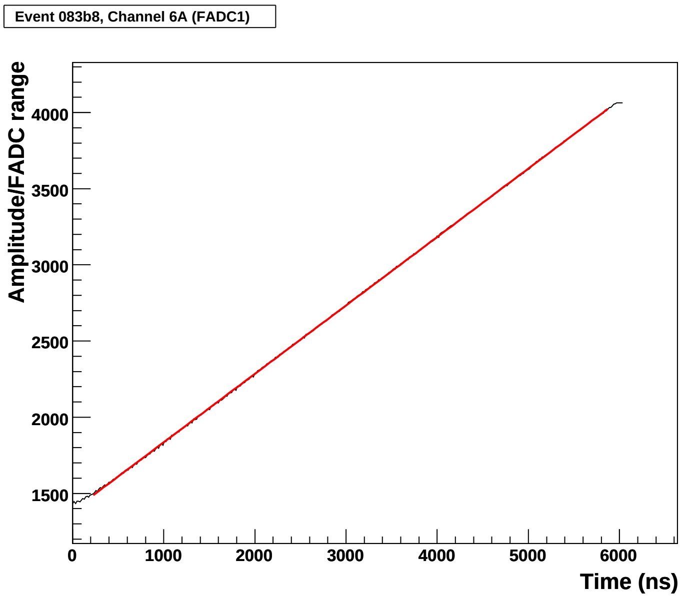

(a)

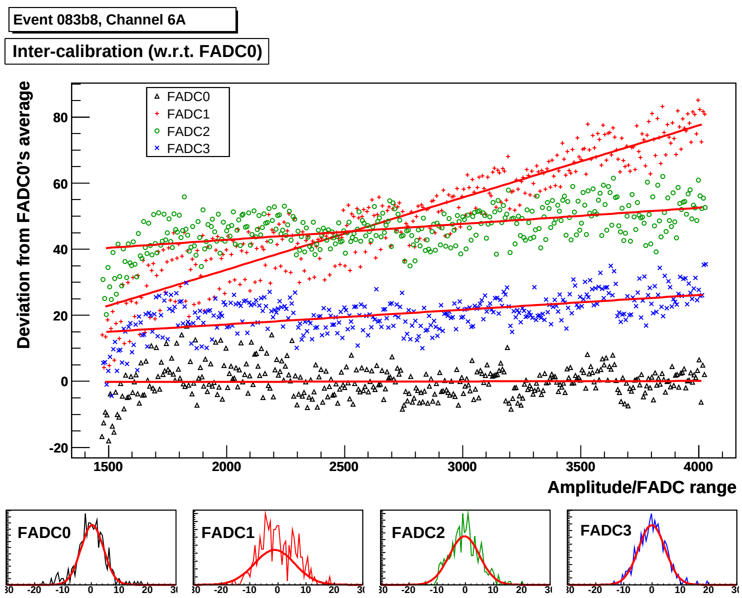

(b)

Figure 4.3: Inter-calibration of FADC data: (a) shows a linear fit of the reference set ($FADC_0$) used for determining the calibration functions. (b) shows the calibration fits with the waveform amplitudes (FADC units) on the independent axis and the relative offsets of the other datasets w.r.t. the reference line on the dependent axis. The line $x = 0$ represents the reference line of (a), with the $FADC_0$ dataset distributed around it as shown. The histograms (bottom) corresponding to the four datasets have a Gaussian distribution in each case.

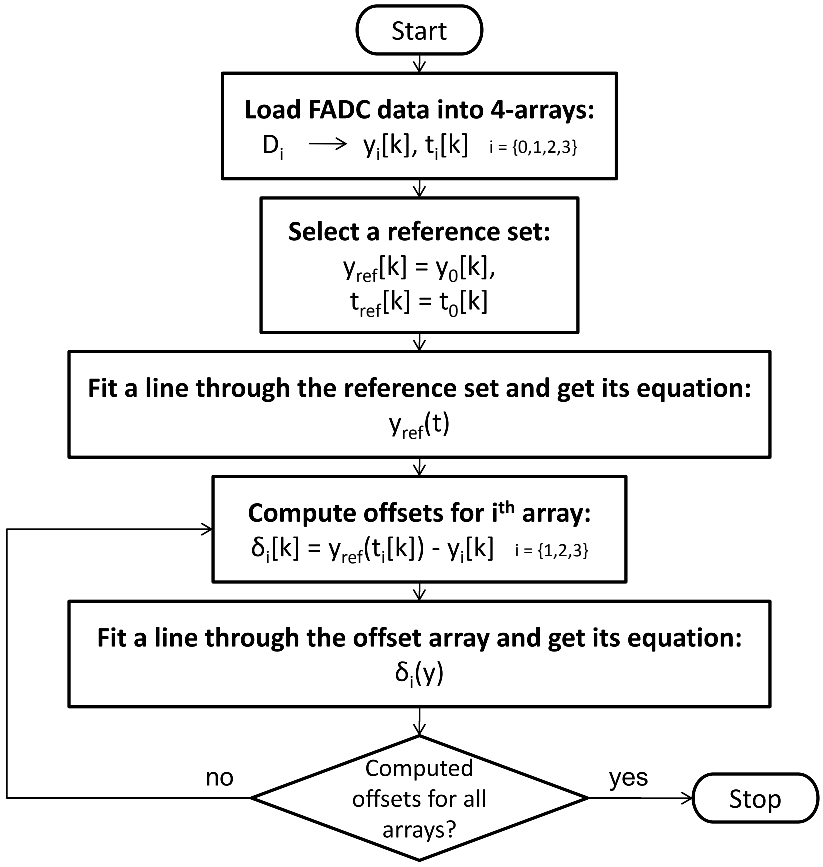

Figure 4.4: Inter-calibration process flowchart: D_i is the output of the i^{th} FADC, where $i = 0, 1, 2, 3$. Here the first FADC's dataset ($i = 0$) is used as the reference set. $y[k]$ and $t[k]$ are integer arrays that carry signal amplitude and time data from the FADCs. k is the index of the data within the arrays: wherever shown in the flowchart, it indicates that the step is to be repeated for each data point k. At the end of the process, three calibration functions, $\delta_1(y)$, $\delta_2(y)$ and $\delta_3(y)$ are obtained.

- A signal's base line was determined as shown in fig. 4.8. All digitized signals have a requisite delay of about 200 ns due to the long SHV cables (described in section 3.5). This delay was not unwanted and it helped in determining the signal's base line. The signal's first 200 ns and last 248 ns were used to fit a zero-slope line through it as shown. However, there are some problems in determining the base line.

  - Sometimes there are event pile-ups, i.e. there are events wherein a signal is riding on top of another signal's trailing edge. This can happen if the event rate is too high. Such signals are hard to detect and eliminate at the analysis stage. Although this situation was controlled by setting the discriminator level high enough to only trigger on large signals, such double signals were still observed in the dataset. Since they could not be detected by the program script, they had an uncertain effect on the signal time measurements. The event selection will be improved in future.

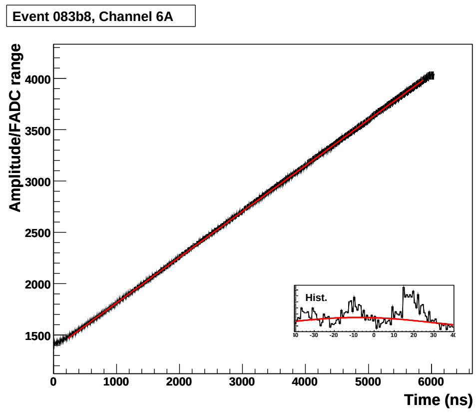

(a)

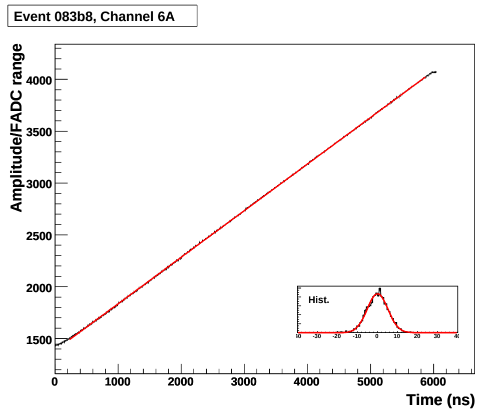

(b)

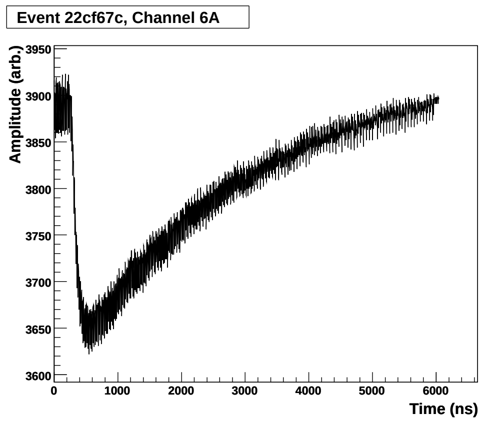

(c)

Figure 4.5: Results of the inter-calibration: (a) shows the original calibration waveform (triangular). Its histogram shows a standard deviation of $\sigma > 40\,\mathrm{LSB}$. (b) shows the same after the calibration. The resulting histogram is a Gaussian with $\sigma \approx 5\,\mathrm{LSB}$. This is comparable with $\sigma \sim 3.4\,\mathrm{LSB}$ of the random noise of the corresponding analog waveform. (c) shows the calibrated version of the signal shown in fig. 4.2(a) (noise $\sigma \sim 10\,\mathrm{LSB}$).

  – A signal has a long falling edge followed by an undershoot (not visible in the figures shown here due to the finite range of the system). The base line level on the falling edge is not pronounced. The base line level before the signal's rising edge is visible, but it provides too low statistics for fitting. For this reason, the above method uses both sides of the signal for fitting a base line, which add to its systematic uncertainty (assumed to be equal to the signal's RMS noise $\sim 10\,\mathrm{LSB}$).

- Next, the signal's peak amplitude was determined. First the signal data was searched for its maximum amplitude point (actually the minimum amplitude point, as the signals are negative). Then a zero-slope line was fitted around that point to get a mean value as shown in fig. 4.8. For fitting, a range of $\pm 100\,\mathrm{ns}$ around the maximum amplitude point was used. The signal's peak amplitude was then computed as the difference between the mean value and the base line. The systematic errors of the mean value and the base line were added in quadrature: $\sqrt{10^2 + 10^2}\,\mathrm{LSB} = 14\,\mathrm{LSB}$. This first, rough determination of the maximum amplitude will be improved in future by e.g. a parabolic fit.

- The rise time was determined by fitting a line between 10 % and 90 % of the signal's peak amplitude on the rising edge. Then the projection of the line-segment (defined by the two limits) on the time-axis was considered as the rise time.
  - Due to signal noise, the fitting range selection was ambiguous, i.e. for two given amplitude levels, several combinations of data points could be considered as candidates to define a data range. This ambiguity was resolved by considering the inner most data points between the two amplitude levels to define the fitting range. This is especially important for the rise time measurement, since the extremes of the fitting range may have non-linear edges and this can affect the systematic uncertainty of the results. This will be determined in future.
- The fall time measurement was done in a similar fashion, except that in this case the fit cannot be linear. The following decay law was used for fitting:

$$y = y_0 - ae^{(-bt)}, \tag{4.3}$$

  where $y = y_0$ is the base line level of the signal and a and b are free parameters (parameter initialization: $a = 300$, $b = 0.0003$).

The results of the measurements of the example signal shown in fig. 4.8 are tabulated in table 4.1. The base line and peak amplitude have systematic errors of $\pm 10\,\mathrm{LSB}$ and $\pm 14\,\mathrm{LSB}$, respectively, that dominate their statistical errors. The rise time and fall time measurements are discussed next.

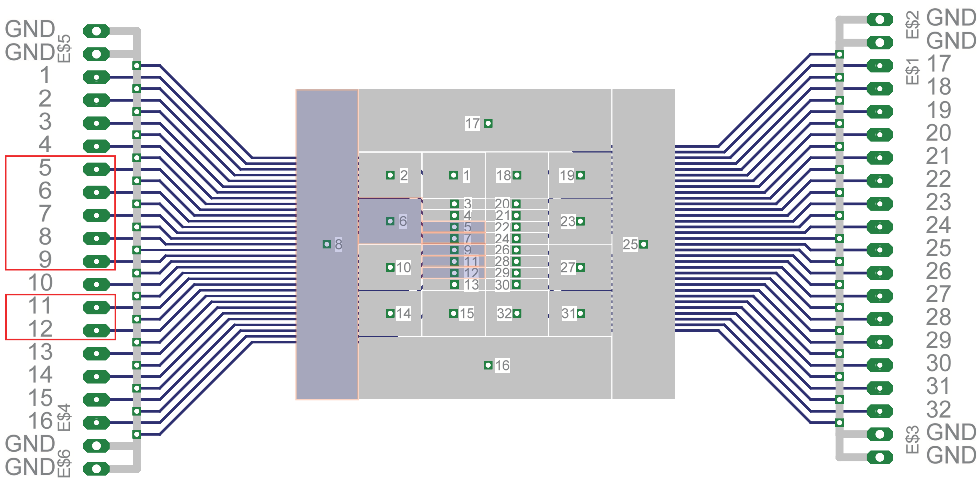

Figure 4.6: The figure shows the pad numbering scheme and the corresponding connections. Only the highlighted pads were used for the analysis (pad numbers 5, 6, 7, 8, 9, 11 and 12). The pad sizes are discussed in section 3.1 [44].

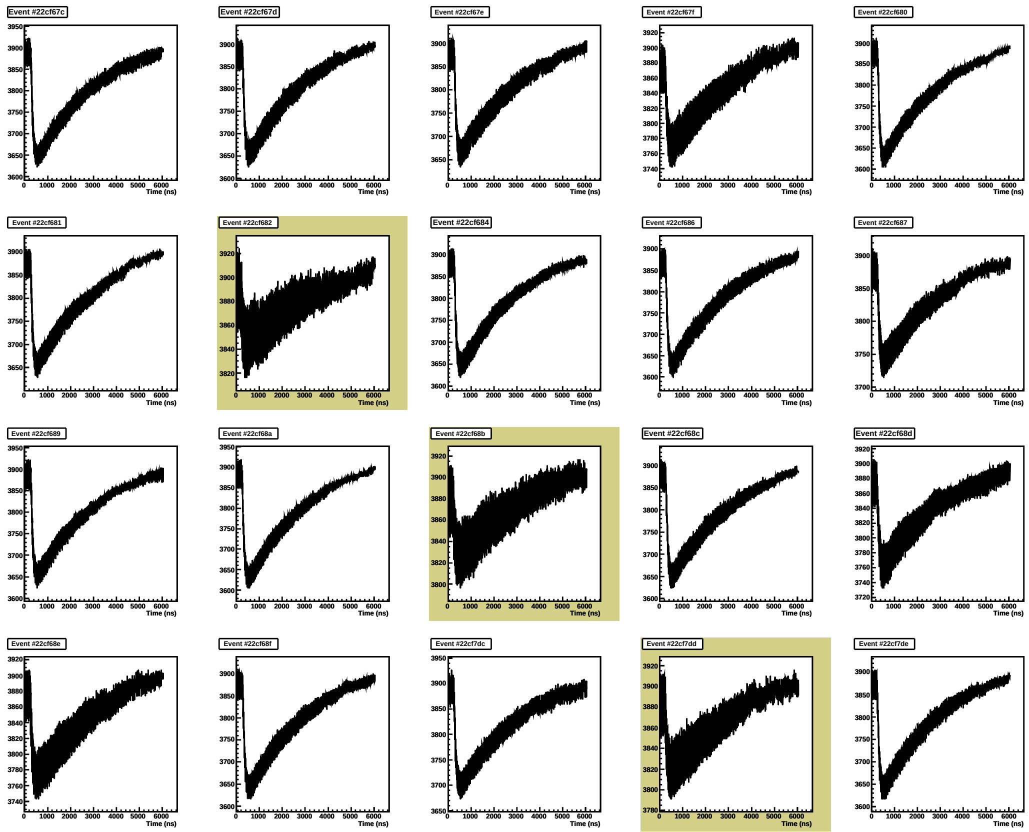

Figure 4.7: Event selection: the figure shows 20 events from a dataset. Signals too low in amplitude are noisy and are therefore unfit for rise time and fall time measurements. The three highlighted event were discarded by the script used for signal time measurements. Notice the different scales of the vertical axes. Only signals with their peaks falling below the threshold value of 3750 arb. units were selected (6707 events from a total of 9113 events).

4.3.1 Rise Time

The positive ions generated during gas amplification within the GEMs drift towards the cathode, and they do not contribute to the signals on the pads. The reason for this is the electrostatic shielding effect of GEM_1. Hence, the signals induced on the pads are due to electrons in the induction gap only.
The Fe^{55} source generates point ionization in the test chamber. When point-like charge distributions drift, they induce a constant current through the pads. Hence, the charge on the pads grows linearly with time ($I = dQ/dt$), up to a time defined by τ_c. τ_c is called the characteristic time of the detector and it can be calculated as:

$$\tau_\mathrm{c} = \frac{d_\mathrm{I}}{\langle v_\mathrm{d} \rangle}, \tag{4.4}$$

where $\langle v_\mathrm{d} \rangle$ is the average drift velocity and d_I is the induction gap spacing. For $d_\mathrm{I} = 0.2\,\mathrm{cm}$ and $\langle v_\mathrm{d} \rangle \approx 5\,\mathrm{cm}/\mu\mathrm{s}$, the characteristic time τ_c is about 40 ns. The observed rise time is expected to be of similar order of magnitude.
The measured rise time of the signal shown in fig. 4.8 was calculated to be 116 ns

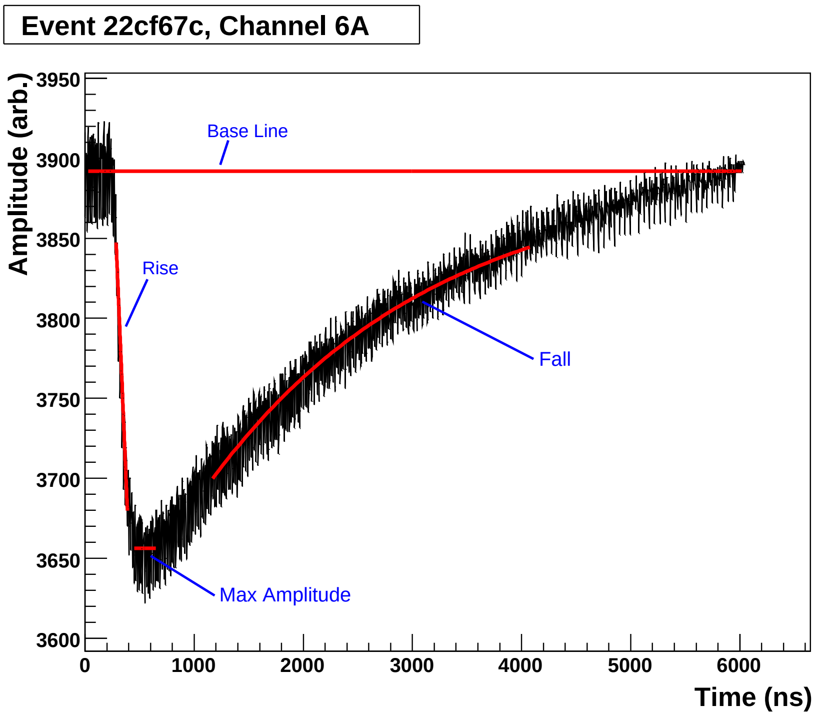

Figure 4.8: Signal measurements: the first step involves fitting of the signal data to determine a base line. Next, the signal's peak amplitude is determined as shown. The rise time and fall time are obtained by fitting this signal data between 10 % and 90 % of the signal's peak amplitude. For the rise time the fit is linear. For the fall time the fitting is performed using equation 4.3.

with an uncertainty of 35 %. The uncertainty is large, because there is too little available statistics. One way around the problem is to try a large number of measurements and check their average value. Hence, the measurements were repeated for a large number of events (6707 events) and the resulting rise times were plotted as a function of signal amplitude. This is as shown in fig. 4.9 for different pad sizes (pad numbers 6, 8 and 9). Their average values are listed in table 4.2. The rise times are almost independent of the signal amplitudes (or the pad sizes), with a slight drop towards the lower amplitudes. Notice the distribution of the data points in fig. 4.9(c) due to the distinct Fe^{55} peak (more on this later).

4.3.2 Fall Time

The fall times of signals due to electrons are generally of the order of a few hundred nanoseconds. However, the fall time of the signal shown in fig. 4.8 was measured to be 4.57 μs (statistical error less than 2 %). This is due to the pre-amplifier electronics. From the circuit diagram shown in fig. C.4 in appendix C, the time constant due to the coupling capacitor C_{32} (100 nF) and the resistor R_{25} (51 Ω), can be calculated to be $\tau = 5\,\mu$s. This has an effect on the output of the pre-amplifier, giving the signal its unusually long tail. Fig. 4.10 shows the distribution of the fall times from a large number of events (6707 events), plotted as a functions of signal amplitude,

Base line		(3892.00	$\pm$0.09 (stat.)) LSB
Peak amplitude		(3656.00	$\pm$0.14 (stat.)) LSB
Rise time	$t_1 =$	(271.80	$\pm$23.62 (stat.)) ns
	$t_2 =$	(388.00	$\pm$33.72 (stat.)) ns
	$t_2 - t_1 =$	(116.20	$\pm$41.17 (stat.)) ns
Fall time	$t_3 =$	(958.70	$\pm$30.61 (stat.)) ns
	$t_4 =$	(5526.00	$\pm$77.71 (stat.)) ns
	$t_4 - t_3 =$	(4567.00	$\pm$83.52 (stat.)) ns
	$y_0 =$	3891	(fixed) LSB
	$a =$	(337.90	$\pm$0.34 (stat.)) LSB
	$b =$	(486.30	$\pm$0.47 (stat.)) $\cdot 10^{-6}\,\mathrm{ns}^{-1}$

Table 4.1: Measurement results of the example signal shown in fig. 4.8.

Pad 9 ($6.8 \times 1.1\,\mathrm{mm}^2$)	(107.82	$\pm$0.03 (stat.)) ns
Pad 6 ($6.8 \times 4.9\,\mathrm{mm}^2$)	(110.74	$\pm$0.02 (stat.)) ns
Pad 8 ($34.1 \times 27.8\,\mathrm{mm}^2$)	(110.68	$\pm$0.02 (stat.)) ns

Table 4.2: Rise times of signals for different pad sizes. These are the averages from the graphs shown in fig. 4.9.

for different pad sizes (pad numbers 6, 8 and 9). Their average values are listed in table 4.3. As expected, the fall times are independent of the signal amplitudes.
The rise time and the fall time measurements discussed above, do not compare with their estimates. This is, because the measurements were performed directly on the pre-amplifier signals. The signals are a convolution of the actual detector signals with the pre-amplifier's response function. The response function must be determined and the necessary deconvolution performed, in order to get the correct rise time and fall time values. These corrections could yet not be carried out due to the time constraint on this thesis.

Pad 9 ($6.8 \times 1.1\,\mathrm{mm}^2$)	(4398.59	$\pm$0.03 (stat.)) ns
Pad 6 ($6.8 \times 4.9\,\mathrm{mm}^2$)	(4424.38	$\pm$0.02 (stat.)) ns
Pad 8 ($34.1 \times 27.8\,\mathrm{mm}^2$)	(4300.74	$\pm$0.02 (stat.)) ns

Table 4.3: Fall times of signals for different pad sizes. These are the averages from the graphs shown in fig. 4.10.

4.3.3 Amplitude

The signal amplitude measurement was already demonstrated in the preceding sections. For all the measurements described above, signals with large amplitudes were used and the other events were ignored. This section compares the distribution of the signal amplitudes from different pad sizes using all the events from the datasets. The data need not be inter-calibrated for this purpose.
Signal amplitudes were measured as described earlier and they were histogrammed. Fig. 4.11 shows the spectra from the three different sized pads (pad numbers 6, 8 and 9). The corresponding MCA spectra are also shown for sake of comparison

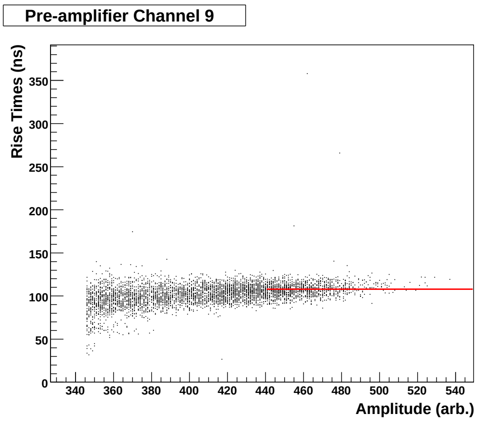

(a) Pad area: $6.8 \times 1.1\,\mathrm{mm}^2$

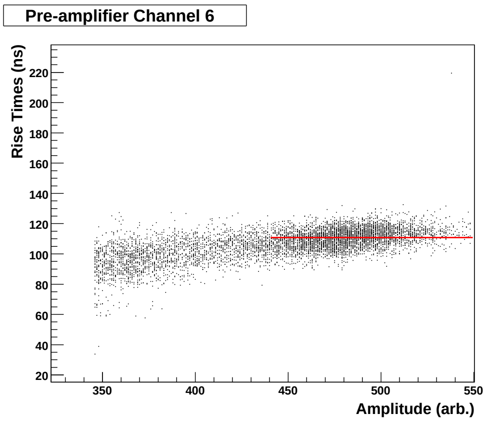

(b) Pad area: $6.8 \times 4.9\,\mathrm{mm}^2$

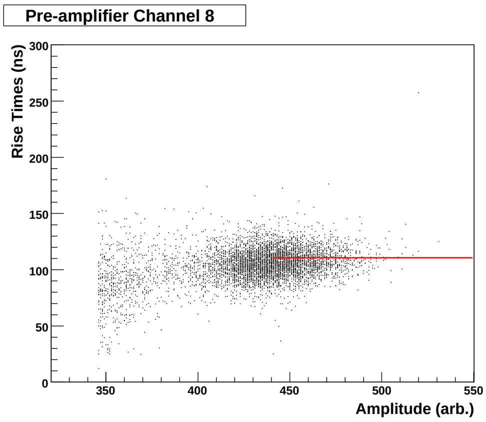

(c) Pad area: $34.1 \times 27.8\,\mathrm{mm}^2$

Figure 4.9: Rise times of signals from different pad sizes: (a) shows signal rise times as a function of amplitude for the smallest pad size. (b) and (c) show the same for the medium and the large size pads, respectively. The rise times are almost independent of the signal amplitudes or pad sizes. The smallest pad shows the best of the results (almost linear). The lines indicate the averages in each case (see table 4.2). Only large amplitudes were considered for averaging, because of their lower variance.

(higher statistics). Notice the empty bin leftwards of the spectrum in fig. 4.11(a). These signals were not registered by the DAQ system because they were blocked by the discriminator. The same holds for the spectra shown in fig. 4.11(c) and fig. 4.11(e).

The signals on the pads are mainly produced by induction due to the drifting charges within the detector. However, a signal on one pad may also induces signals on the neighboring pads (cross-talk), in which case the amplitude would depend on the level of induction. For example, the spectrum in fig. 4.11(a) is not as clean as in fig. 4.11(e). This is, because the larger the pad's area, the more is the probability that it generates a signal due to drifting charges in the detector, while the chances of induction due to its surrounding pads are comparable to that of the smaller pads.

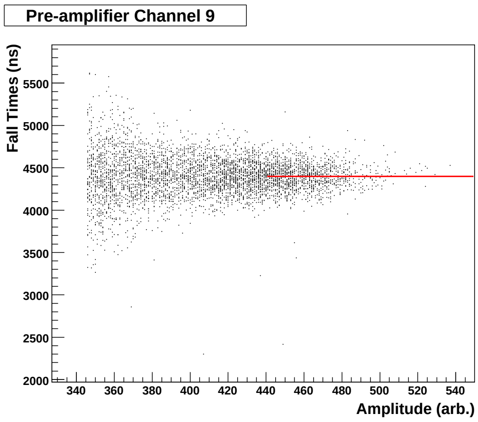

(a) Pad area: $6.8 \times 1.1\,\mathrm{mm}^2$

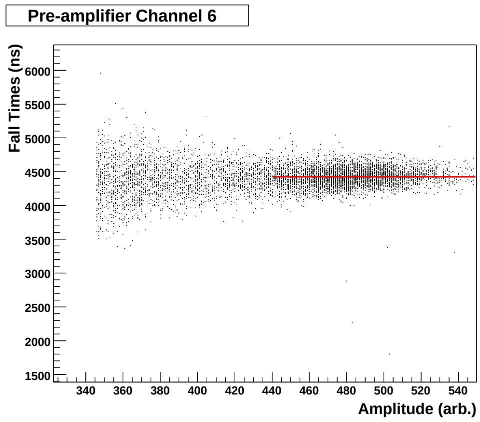

(b) Pad area: $6.8 \times 4.9\,\mathrm{mm}^2$

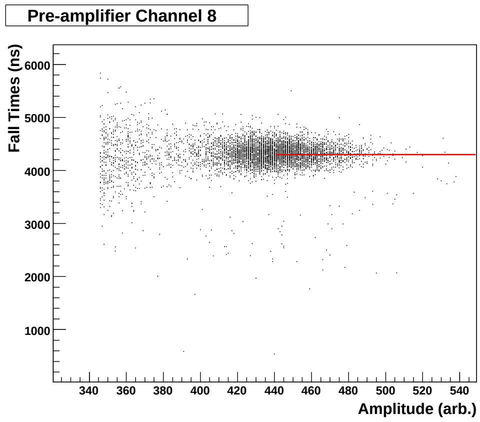

(c) Pad area: $34.1 \times 27.8\,\mathrm{mm}^2$

Figure 4.10: Fall times of signals from different pad sizes: (a) shows signal fall times as a function of amplitude for the smallest pad size. (b) and (c) show the same for the medium and the large size pads, respectively. As expected, the fall times are independent of the signal amplitudes. The lines indicate the averages in each case (see table 4.3). Only large amplitudes were considered for averaging, because of their lower variance.

4.4 Signal Sharing Between Adjacent Pads

The main objective in studies of GEM based TPCs with pad readout is to achieve good spatial resolution, in order to determine the azimuthal coordinate of the ionizing particles in the detector very precisely. There are two ways of achieving this: by reducing the pad size; or by spreading the charge after the gas gain over multiple pads and use a center-of-gravity method to determine their position coordinates. The pad sizes are limited due to the difficulties in implementing the complex readout electronics for extremely small pads. However, the charge spreading technique can be employed to provide a position resolution better than the pad size.
If the electrons are collected on a single pad, the center-of-gravity method cannot be used. In such a case the maximum resolution is given by a box shaped distribution, $\sigma_{\mathrm{B}} = \delta x/\sqrt{12}$, where δx is the pitch of the pads. However, if the charge is spread over multiple pads the maximum resolution is given by a Gaussian distribution of

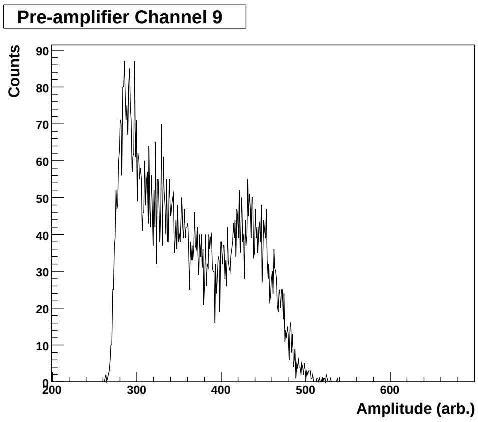

(a) Pad area: $6.8 \times 1.1\,\mathrm{mm}^2$

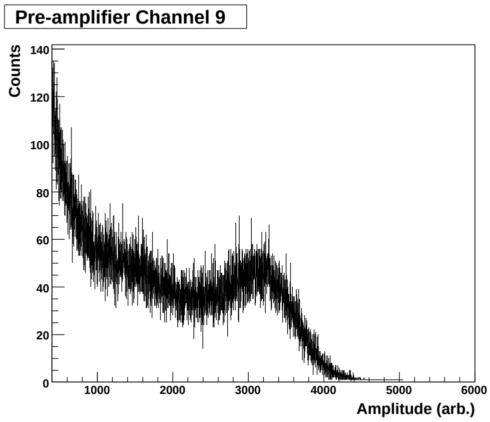

(b) MAC spectrum of ch. 9

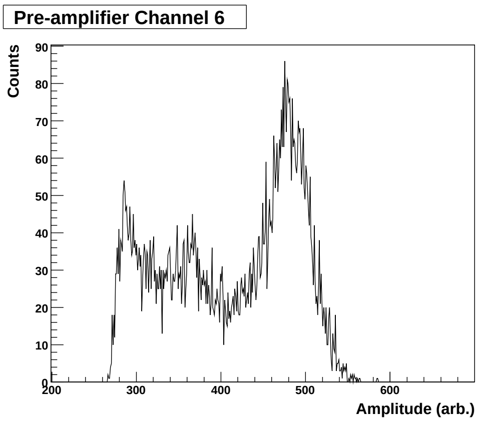

(c) Pad area: $6.8 \times 4.9\,\mathrm{mm}^2$

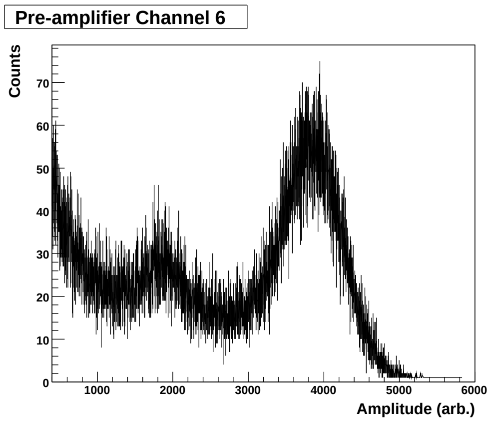

(d) MAC spectrum of ch. 6

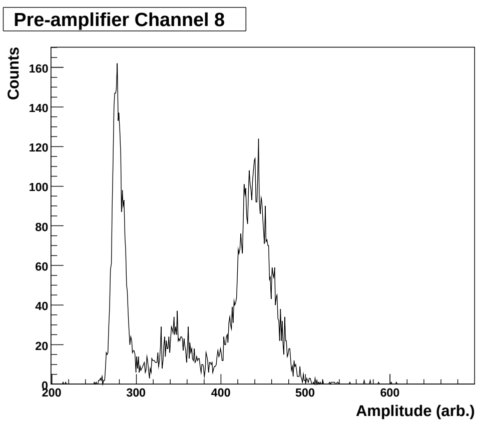

(e) Pad area: $34.1 \times 27.8\,\mathrm{mm}^2$

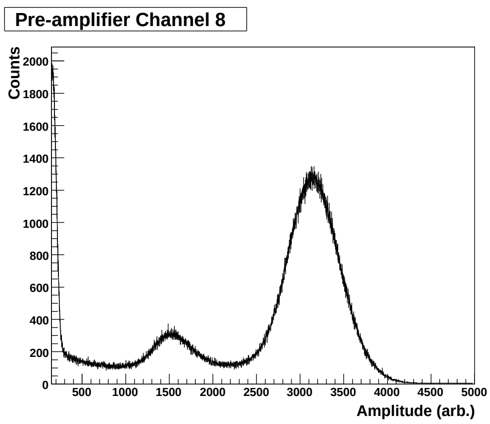

(f) MAC spectrum of ch. 8

Figure 4.11: Comparison of amplitude spectra from different pads. (a) shows the amplitude spectrum of the smallest pad developed from the FADC dataset. (b) shows the corresponding MCA spectrum for comparison. Similarly, (c) and (e) are spectra of larger pads and (d) and (f) are their corresponding MCA spectra, respectively.

the signal shared between the pads, having a spread, $\sigma_G = \Delta x/2.355$, where Δx is the full width at half maximum (FWHM) of the Gaussian.

An experiment was performed to measure the signal sharing between adjacent pads. A row of five identical pads was chosen (pad numbers 5-7-9-11-12). Their amplifier outputs were connected to the digitizer board inputs by means of long delay cables. The center most pad (pad 9) was chosen for the trigger signal generation (refer to section 3.5 for details). A collimated radioactive source was placed on top of the test chamber window. Its position was adjusted until simultaneous signals were observed on all five pads. In this way a large dataset was collected.

The mobility of electrons in an Ar-CO_2 gas mixture, at a drift field of about 1 kV/cm, is $\mu_e \approx 5 \cdot 10^3\,\mathrm{cm^2V^{-1}s^{-1}}$. Using equation 2.5, the diffusion coefficient at room temperature can be estimated to be $D \approx 1.3 \cdot 10^{-4}\,\mathrm{cm^2/\mu s}$. Hence, the diffusion width is $\sqrt{2Dt} \approx 0.05\,\mathrm{mm}$ (assuming a drift time $t = 100\,\mathrm{ns}$). For this experiment, the width of the charge clusters incident on the pads can be assumed to be of the same order. Since an entire cluster is collected on a single pad (width 1.1 mm), the center-of-gravity method does not apply here.

The signal amplitudes of all five pads were determined for an event. The amplitudes were corrected for the gain differences between pre-amplifier channels and the different damping factors due to the delay cables. A histogram of the corrected amplitudes from a single event is shown in fig. 4.12. It shows that the center most pad was hit and signals were induced on the neighboring pads. In this case the maximum position resolution is given by $\sigma_B = 0.36\,\mathrm{mm}$ (with the pads having a pitch of 1.25 mm).

The observed distribution could be due to several reasons, the first being the noise level of the signals from the neighboring pads. The digitization process introduces an uncertainty (± 10 LSB) in determining their amplitudes. In the histogram the amplitudes of these pads could be due to the signal noise itself. The pre-amplifier cross-talk could be another factor affecting their amplitudes (the measured cross-talk level was about 4 %). A more detailed experimental work is necessary to understand the behavior of the system and to tune it get reliable data.

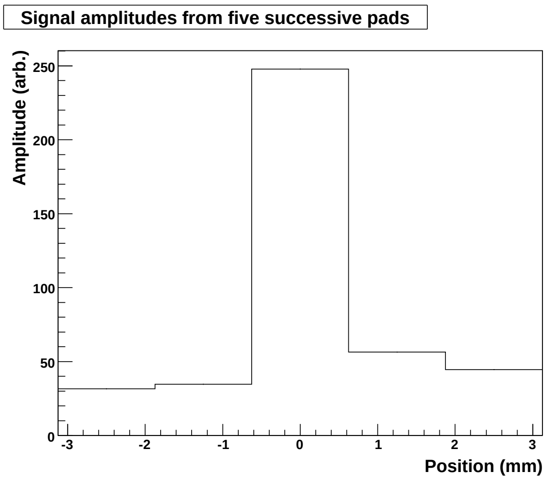

Figure 4.12: A histogram of signal amplitudes from adjacent pads (corresponding to a single event) showing the sharing of the signal.

Chapter 5

Conclusions and Outlook

In this thesis the reconstruction of signals from a GEM based detector, with pad readout, using a time interleaved FADC system has been discussed. This technique allows high-resolution sampling of detector signals. The reconstruction of signals was successfully tested with 4 ns resolution. A simple method was devised for inter-calibration of the FADC data for further analysis. The method successfuly reduced the signal noise introduced due to the interleaved FADCs by 40 %. However, a better method is needed for a systematic correction of the FADC mismatch errors to make proper use of the system's capabilities. For example, references [43, 45] suggest some approaches.

The system allows both online and offline processing of data. An attempt was made to measure the signal rise times and fall times from the stored event data. The measurements do not agree with their estimates, because of the signal shaping done by the pre-amplifiers. More experimental work is required to study the response of the pre-amplifiers and determine the actual rise time and fall time of the detector signals.

The system can also combine data from different channels, and provide position information of the ionizing events. However, its resolution is limited by the pad width ($\sigma_{\mathrm{B}} = 0.36\,\mathrm{mm}$). More experimental work is required to study the signal sharing between pads, and use the center-of-gravity method to improve the position resolution.

Although the detector system, as of now, lacks the flexibility for an in-depth study of GEMs, the basic functioning of the test chamber and the pre-amplifier electronics was tested. The DAQ system can now be used to study the data from the test chamber or even the TPC prototype. The HV system needs to be upgraded to allow custom settings of the various HVs inside the detectors. Also the possibly to include a third GEM in the setup has to be foreseen. For detailed gas studies with the detectors, a gas mixer must be added to the setup to enable custom selection of quench gas fractions. The work on all these items has already started.

Appendix A

Test Chamber Settings and Calculations

A.1 Test Chamber Settings

This section summarizes the various test chamber settings used for the measurements described in this thesis.

Pre-amplifiers, digitizer channels, and delay cables: The signal time and amplitude measurements were performed for three different pads. The pre-amplifier channel numbers correspond to the pad numbers. For each of these measurements the same digitizer channel (channel 6A) and delay cable were used. However, in the measurements described in section 4.4, signals from five pads were simultaneously digitized. Table A.1 lists the pre-amplifier channels, their gains, cable losses and the corresponding digitizer channels used. Note that each digitizer board provides two channels. For example, the first channel on digitizer board number 5 is named 5A, the second channel 5B and so on.

Pre-amplifier Channel	**Gain (%)** g_i^{amp}	**Cable Loss (%)** g_i^{cable}	**Cable Delay (ns)**	**Digitizer Channel**
5	23.4	0.87	418	5A
7	23.6	0.88	420	5B
9	23.8	0.88	420	6A
11	24.0	0.87	414	6B
12	25.2	0.88	418	7A

Table A.1: The pre-amplifiers, their gains, the delay cable properties and the digitizer channels used in the measurements described in section 4.4.

The amplitudes of signals from each channel were corrected for different pre-amplifier gains and delay cable losses. If y_i is the peak amplitude of the digitized signal, then the true amplitude is calculated as:

$$y_i^{'} = y_i(\frac{g_9}{g_i}),$$

where $i = \{5, 7, 9, 11, 12\}$ is the channel number and g_i is the effective gain factor (pre-amplifier gain and cable loss):

$$g_i = g_i^{\text{amp}} g_i^{\text{cable}}.$$

See table A.1 for the values of g_i^{amp} and g_i^{cable}.

Other settings: Table A.2 lists the various test chamber settings (HV setting and geometrical parameters).

Cathode:	$V_{\text{cathode}} = -2212 \pm 1\,\text{V}$
Divider:	$V_{\text{divider}} = -1700 \pm 1\,\text{V}$
GEM_2 cathode:	$V_{\text{GEM2c}} = -1314 \pm 1\,\text{V}$
GEM_2 anode:	$V_{\text{GEM2a}} = -1008 \pm 1\,\text{V}$
GEM_1 cathode:	$V_{\text{GEM1c}} = -665 \pm 1\,\text{V}$
GEM_1 anode:	$V_{\text{GEM1a}} = -360 \pm 1\,\text{V}$
Anode:	$V_{\text{anode}} = 0\,\text{V}$
Drift length (Cathode to GEM_2):	$d_{\text{D}} = 5\,\text{mm}$
Transfer gap (GEM_2 to GEM_1):	$d_{\text{T}} = 2\,\text{mm}$
Induction gap (GEM_1 to pad plane):	$d_{\text{I}} = 2\,\text{mm}$

Table A.2: Test chamber HV settings and geometrical parameters.

A.2 GEM Charge Transfer Coefficients' Estimates

This section illustrates the calculation of the various charge transfer coefficients and the gains of the GEMs (see table A.3), from the voltages listed in section A.1. The various constants used in the calculation are deduced from measurements presented in reference [46], for similar GEMs and drift gas mixtures (refer to section 2.7 for more details).

Drift field:	$E_\mathrm{D} = \dfrac{V_\mathrm{GEM2c} - V_\mathrm{cathode}}{d_\mathrm{D}} = 1796\,\mathrm{V/cm}$
Transfer field:	$E_\mathrm{T} = \dfrac{V_\mathrm{GEM1c} - V_\mathrm{GEM2a}}{d_\mathrm{T}} = 1715\,\mathrm{V/cm}$
Induction field:	$E_\mathrm{I} = \dfrac{V_\mathrm{anode} - V_\mathrm{GEM1a}}{d_\mathrm{I}} = 1800\,\mathrm{V/cm}$
GEM_2 potential deference:	$\Delta V_\mathrm{GEM2} = V_\mathrm{GEM2a} - V_\mathrm{GEM2c} = 306\,\mathrm{V}$
GEM_1 potential deference:	$\Delta V_\mathrm{GEM1} = V_\mathrm{GEM1a} - V_\mathrm{GEM1c} = 305\,\mathrm{V}$
Hole field of GEM_2	$E_\mathrm{hole2} = a\Delta V_\mathrm{GEM2} + b(E_\mathrm{D} + E_\mathrm{T}) = 43.93\,\mathrm{kV/cm}$,
Hole field of GEM_1	$E_\mathrm{hole1} = a\Delta V_\mathrm{GEM1} + b(E_\mathrm{T} + E_\mathrm{I}) = 43.79\,\mathrm{kV/cm}$, where $a = 142.87\,\mathrm{cm}^{-1}$, and $b = 0.0623$
Electron collection efficiency of GEM_2:	$C^-_\mathrm{GEM2} = 1$
Electron extraction efficiency of GEM_2:	$X^-_\mathrm{GEM2} = \dfrac{E_\mathrm{T}/E_\mathrm{hole2}}{T_\mathrm{opt}} + g = 0.2895$, where $T_\mathrm{opt} = 0.1403$, and $g = 0.01127$
Gain of GEM_2:	$G^-_\mathrm{GEM2} = \beta\exp(\alpha\Delta V_\mathrm{GEM2}) = 30.41$, where $\alpha = 0.02129\,\mathrm{V}^{-1}$, and $\beta = 0.04505$
Effective gain of GEM_2:	$G_\mathrm{GEM2} = C^-_\mathrm{GEM2}X^-_\mathrm{GEM2}G^-_\mathrm{GEM2} = 8.802$
Electron collection efficiency of GEM_1:	$C^-_\mathrm{GEM1} = 1$
Electron extraction efficiency of GEM_1:	$X^-_\mathrm{GEM1} = 0.3042$
Gain of GEM_1:	$G^-_\mathrm{GEM1} = 29.76$
Effective gain of GEM_1:	$G_\mathrm{GEM1} = 9.055$
Total effective gain of both GEMs:	$G = G_\mathrm{GEM1}G_\mathrm{GEM2} = 79.71$

Table A.3: Calculation of the charge transfer coefficients.

Appendix B

Time Dependent Systematic Effects in the Interleaved FADC System

The FADC data inter-calibration was described in section 4.2. Fig. 4.5(b) demonstrates the quality of the inter-calibration. The waveform shown in the figure is almost distortion free. However, when the same calibration functions are applied to another signal, that was digitized at another time, the results are not as good. Hence, there are time dependent systematic errors in addition to the offsets and the gains error of the FADCs.

An experiment was performed just to study this special case. Two calibration waveforms (covering only a part of the whole horizontal axis range) were used to compute the calibration functions as described in section 4.2. The calibration waveforms are shown in fig. B.1(a) and fig. B.1(b). Ignore the artifacts on the lower edges of the triangular waveform. They are a consequence of using the FADCs beyond their working range (this was done deliberately to check the full FADC range). The calibration functions were then used to calibrate a test sinusoidal waveform. The results are shown in fig. B.1(c) and fig. B.1(d), respectively (the slanted lines indicate the range described above to get the calibration functions). Notice the distortions in the maxima and the minima of the sinusoidal waveforms. This might indicate some non-linear behavior of the interleaved system. In fig. B.1(e) the same test sinusoidal waveform was calibrated using the regular method described in section 4.2 (using a calibration waveform that covers the whole horizontal axis range). The maxima and the minima of this sinusoidal waveform have lesser distortions. Therefore, the choice of the calibration waveform is very critical for the method of inter-calibration used.

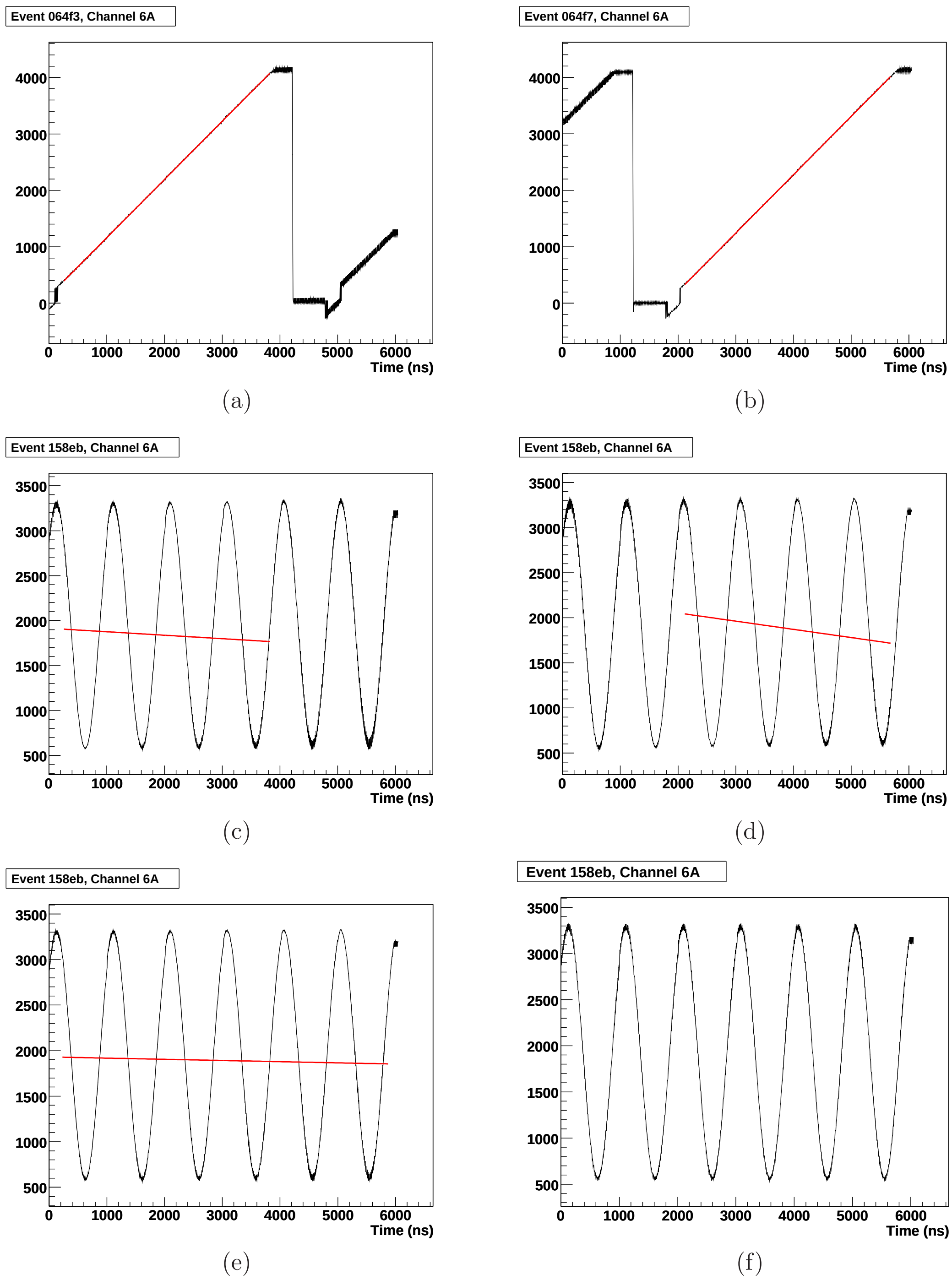

Figure B.1: Figures (a) and (b) show two irregular calibration waveforms that do not cover the whole measuring cycle or the time scale. The examples shown in (c) and (d) were calibrated using (a) and (b), respectively. (e) shows the result, when a regular calibration waveform was used. (f) shows the sinusoidal waveform of (c), (d) and (e) in its original form. Notice the distortions in the maxima and the minima of the sinusoidal waveforms shown in (c) and (d). The results depend on the choice of the calibration waveforms' range. The slanted lines in (c), (d), and (e), have been placed just to show the horizontal range in which the calibration functions were computed.

Appendix C

Setup Components

This appendix summarizes the various setup components, their settings, model numbers etc. (table C.1). The radioactive sources used in the setup are listed in table C.2.
Fig. C.1 shows the geometry of the GEMs used in the setup.
Figs. C.2, C.3, C.4 and C.5 are circuit diagrams of some of the in-house built electronic devices. The other devices are described in references [34, 38, 39].

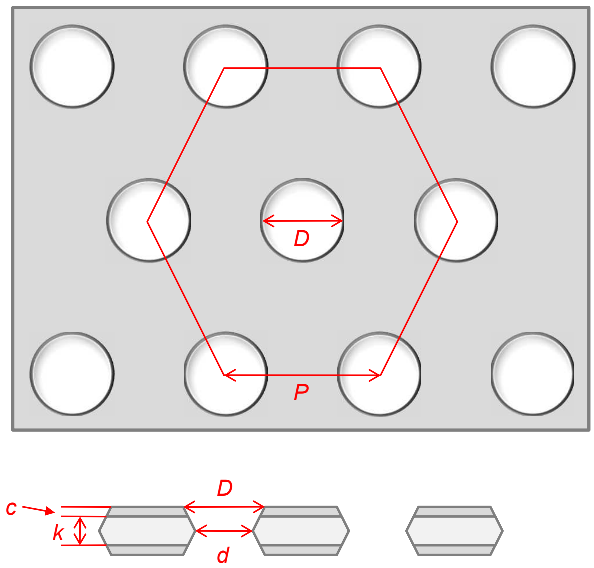

Figure C.1: GEM Geometry: The GEMs used in the setup have a hexagonal hole geometry. The holes have double-conical shape as shown. The holes have a smaller (polyimide) diameter of $d = 50 \pm 5\,\mu$m, a larger (copper) diameter of $D = 70 \pm 5\,\mu$m and a pitch of $P = 140\,\mu$m. The thickness of the polyimide layer is $k = 50\,\mu$m and of both the copper layers is $c = 5\,\mu$m.

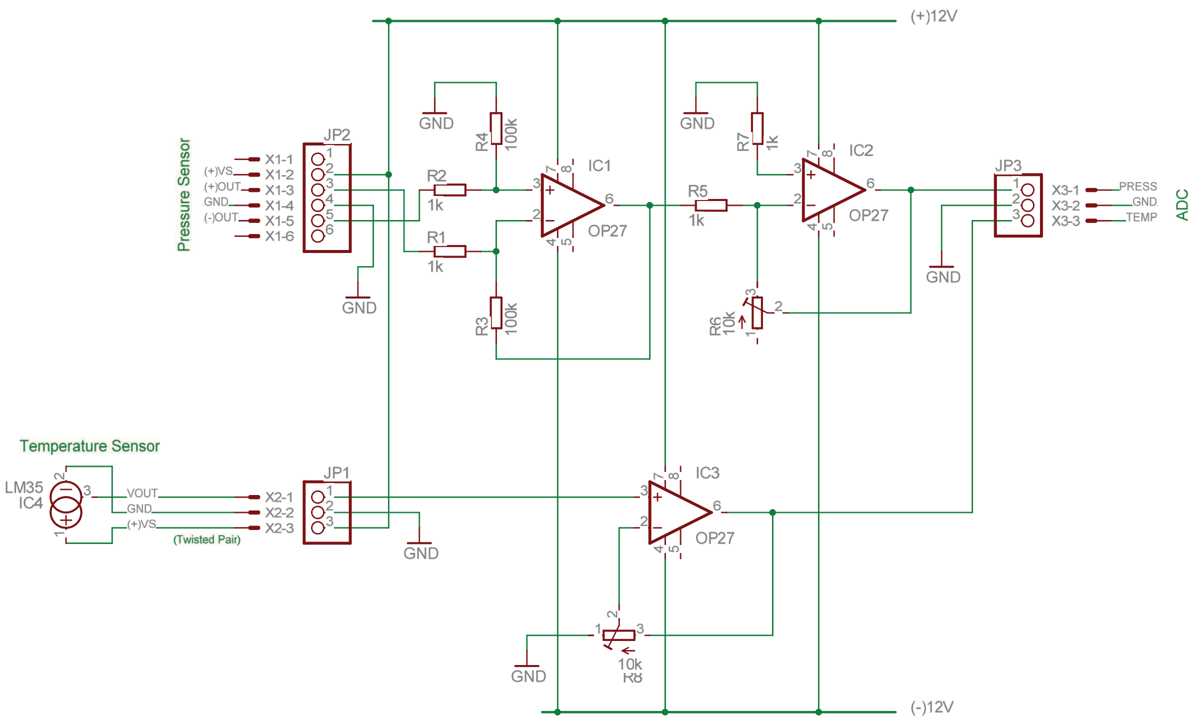

Figure C.2: Temperature and pressure monitor schematic diagram.

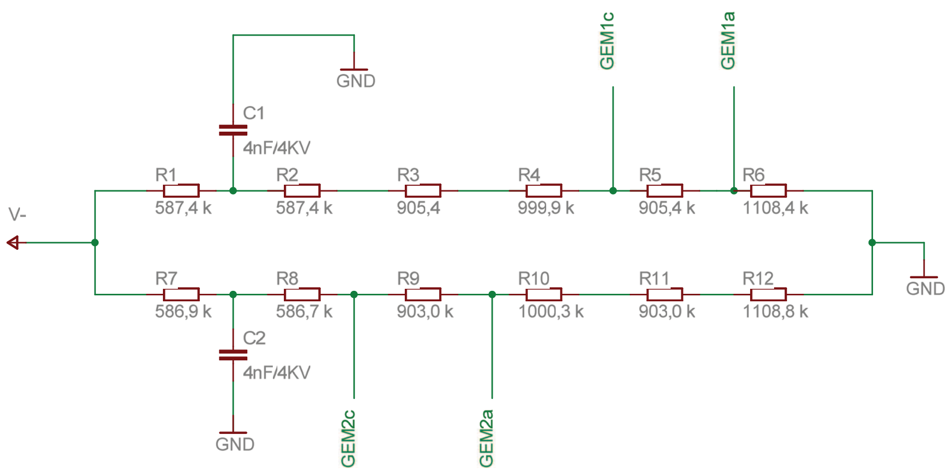

Figure C.3: GEM HV divider circuit diagram: all measurements were performed with $V_{-} = -1700\,\mathrm{V}$. The resistances shown were measured by means of a conventional digital multimeter [37]. The labels "GEM1c" and "GEM1a", for example, indicate GEM_1 cathode and anode voltages, respectively.

Device Name Model	**Manufacturer/** **Comments**	
Gas system in general		
Various parts	FESTO	
Flow meters	GEC-Elliott 1100	
Gain monitor		
HV supply	SILENA 7712	Settings: +1350 Volts
Pre-amplifier		Similar to what is described in [34]
Signal shaper		Similar to what is described in [34]
Main Amplifier	ORTEC Research Amp. 450	Settings: gain 50; 6 Volts output
MCA $ROI = [300, 4300)$	FAST ComTec MCA3A	Settings: 8192 channels;
Temperature and pressure monitor		
Computer interface card	Velleman K8055	Function used: ADC
Pressure sensor	SenSym SCX30AN	Range: 0 bar - 2 bar; absolute type
Temperature sensor	National Semiconductor LM35	Range: +2 °C - +150 $°C$
High-voltage system		
HV supply (Cathode)	CAEN N126	Settings: $V_0 = 2200$ V; current limit 1 mA; ramp speed ~ 2 V/s
HV supply (GEMs)	ISEG NHQ 202M	Output levels are set by software (computer controlled)
Test chamber		
Pre-amplifiers		Gain ~ 25 [44]
Amplifier power supply	Agilent E3648A	Settings: +5 V and −5 V; current limits 200 mA
DAQ system		
Trigger shaper & discriminator		Similar to what is described in [34]
Function generator for calibration	Agilent 33250A	Settings: triangular wave; $f = 200$ kHz; $V_{pp} = 1.3$ V; $V_{off} = -500$ mV
Digitizer & storage electronics		Hardware as described in [38]
PCI acquisition device	AMCC S5935	Hardware as described in [38]
Amplifier (for MCA)	Harshaw NA-17	Gain ~ 160

Table C.1: A list of the devices used in the experimental setup.

Source	Activity	Collimated	Purpose	Internal ID
Fe^{55}	736 MBq	Yes	Test chamber study	Fe55.07.08
Fe^{55}	4 MBq	No	Gas gain monitoring	Fe55.0A.05

Table C.2: A list of the radioactive sources used in the experimental setup. Tabulated in the second column are the calculated estimates of their present activities (as of Feb 2008).

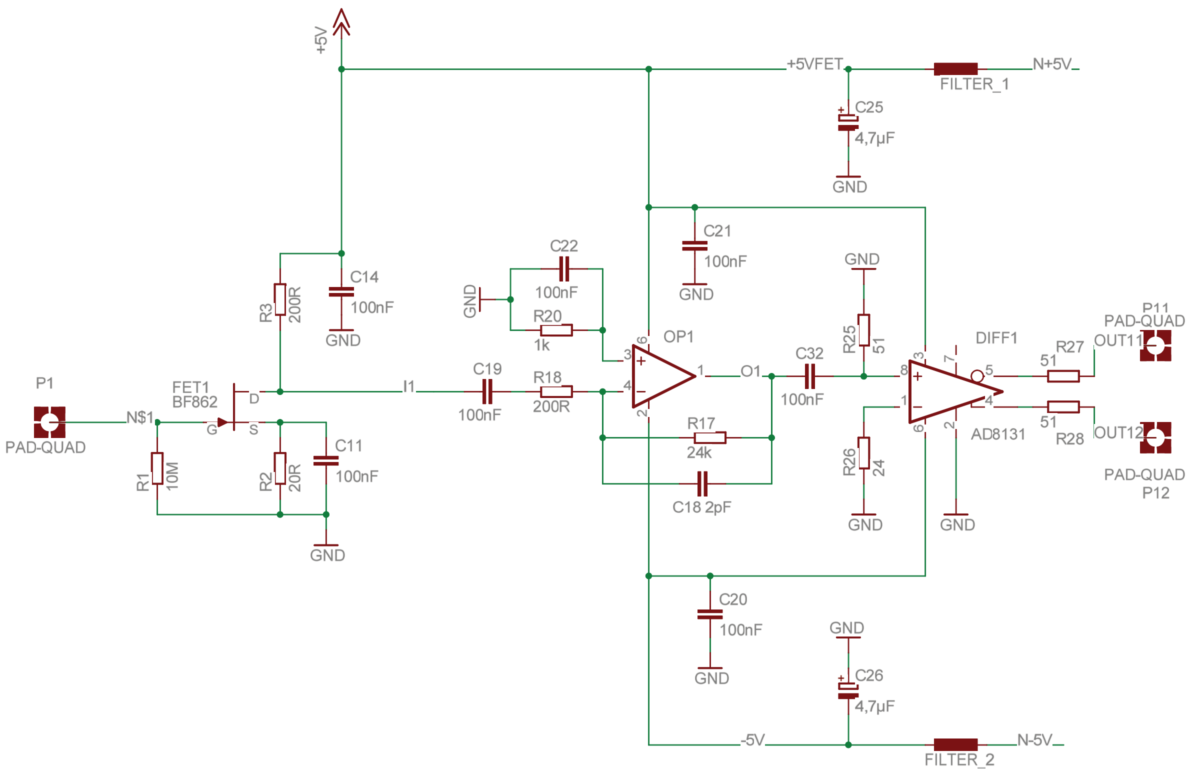

Figure C.4: Test chamber pre-amplifier schematic diagram: the diagram shows a single pre-amplifier channel (gain ~ 25). A total of 7 channels were used. The pre-amplifier sits directly on the pad-board (making contact at pad P1). Amplified signals appear on the output pads P11 and P12 (negative and positive output respectively). These outputs signals are transmitted to the DAQ system by means of shielded twisted-pair cables. The amplifier power filters are as shown in fig. C.5 [44].

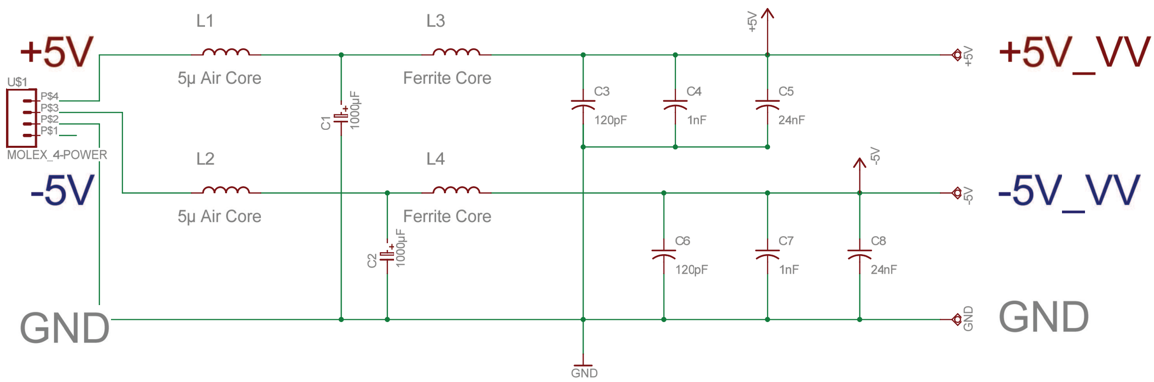

Figure C.5: Test chamber pre-amplifier power filters [44].

Appendix D

Photographs

Fig. D.1 shows the dismantled test chamber assembly. Two of the HV cable connector covers (see section 3.4) have been removed displaying the $20\,\mathrm{M\Omega}$ resistors. The other components are as labeled (see section 3.1 for their description).
Fig. D.2 shows two sides of the gas system. It is mounted on an aluminum plate, which is fixed to a NIM rack. The GMon device is installed behind the gas system. The other parts of the gas system are also mounted in the same rack (not shown).
Fig. D.3 (left) shows the inside of the TPMon device. The pressure sensor is mounted on the circuit board as shown. The temperature sensor is mounted, on the cover of the device, at an end of a long metallic tube (not shown). Fig. D.3 (right) shows the inside of the GMon device with its various components as labeled (see section 3.3 for details).

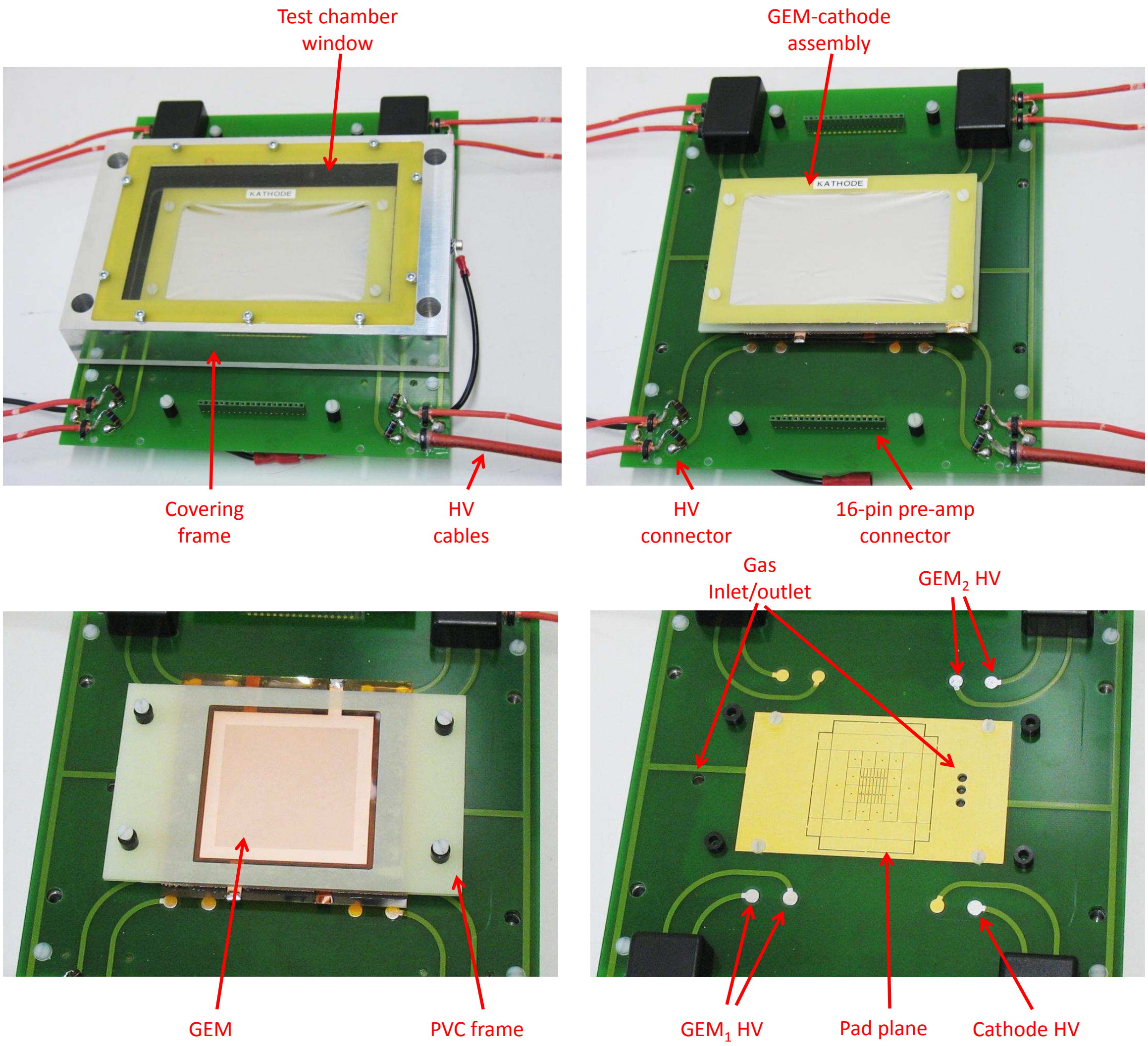

Figure D.1: Test chamber photographs: (top-left) shows the complete assembly, (top-right) GEM-cathode stack (covering frame removed), (bottom-left) GEM stack alone (cathode frame removed), (bottom-right) pad plane only.

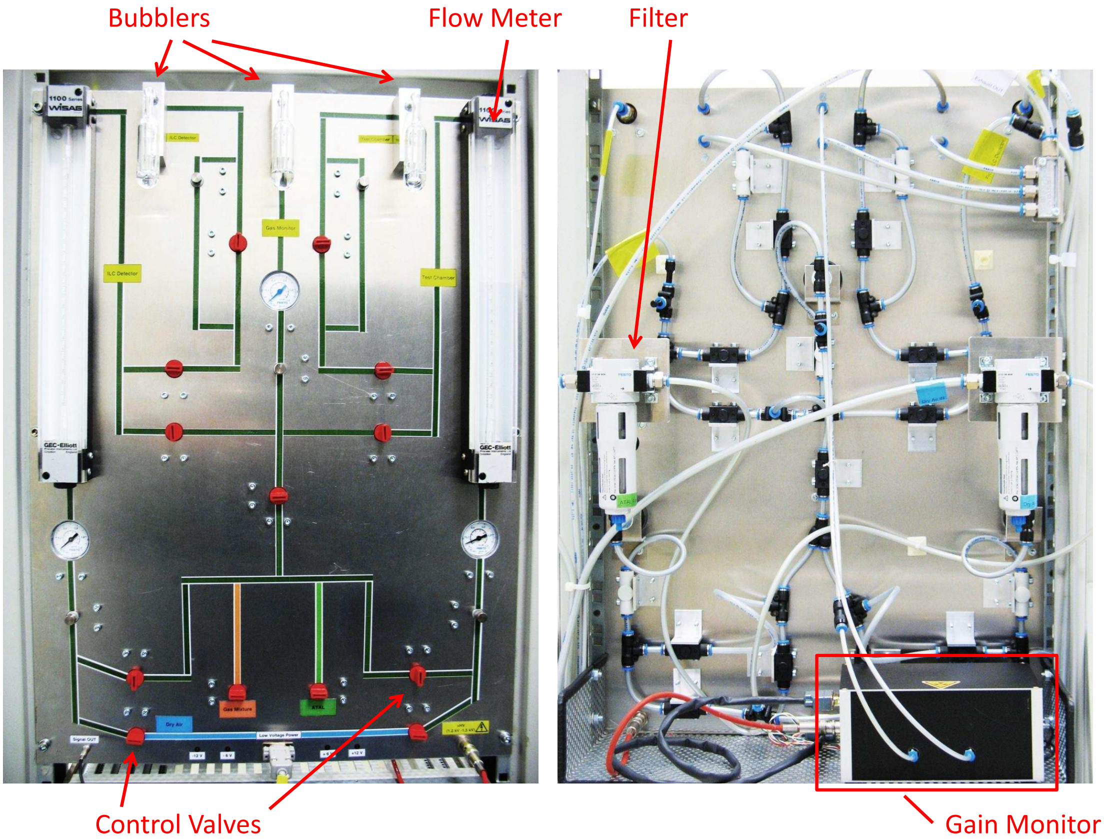

Figure D.2: Gas system photographs: (left) shows the front side, (right) shows the rare side.

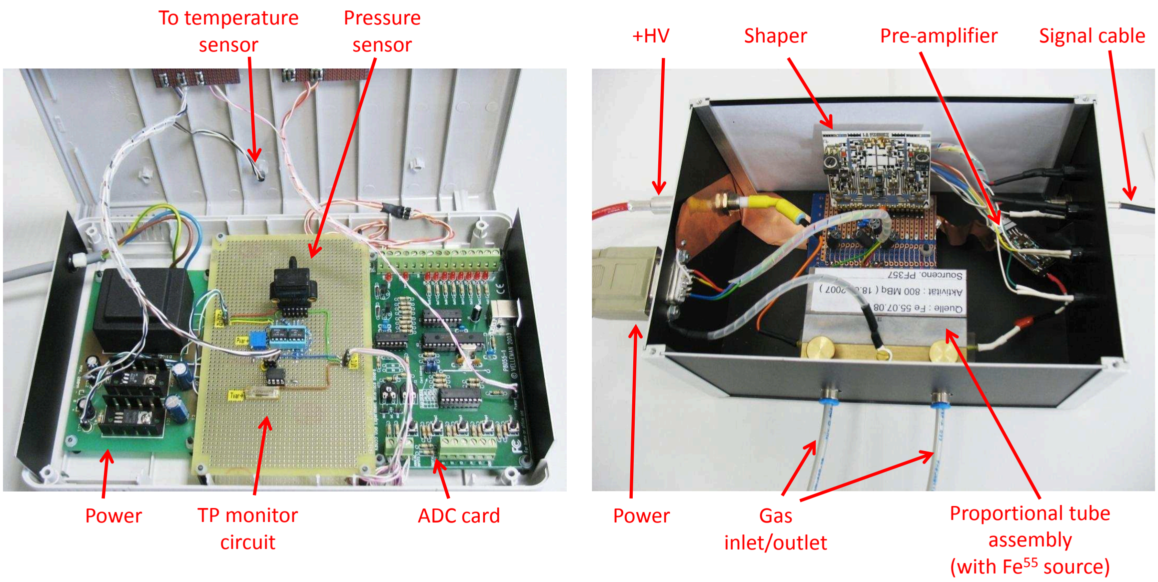

Figure D.3: TPMon and GMon photographs: (left) shows the inside of the temperature and pressure monitor, (right) shows the inside of the gas gain monitor.

List of Abbreviations and Acronyms

ADC .... analog-to-digital converter, page 20
CERN .... Conseil Européen pour la Recherche Nucléaire, page 4
CRC .... cyclic redundancy check, page 30
DAQ .... data acquisition, page 23
DESY .... Deutsches Elektronen-Synchrotron, page 4
ECL .... emitter-coupled logic, page 30
FADC .... flash ADC, page 28
FIFO .... first-in first-out, page 28
FPGA .... field-programmable gate array, page 28
FR-4 .... flame retardant-4, page 14
FWHM .... full width at half maximum, page 52
GEMs .... Gas electron multipliers, page 10
GMon .... gain monitor, page 22
GUT .... grand unification theory, page 2
HV .... high voltage, page 27
ILC .... international linear collider, page 4
LEP .... large electron-positron collider, page 4
LHC .... large hadron collider, page 4
LSB .... least significant bit, page 37
MCA .... multichannel analyzer, page 23
PCB .... printed circuit board, page 14
PVC .... polyvinyl chloride, page 15
QCD .... quantum chromodynamics, page 2
QED .... quantum electrodynamics, page 2
RMS .... root mean square, page 20
ROI .... region of interest, page 23
SCRF .... superconducting radio-frequency linac, page 4
SM .... standard model, page 1
SUSY .... supersymmetry, page 2
TESLA .... TeV-energy superconducting linear accelerator, page 4
TPC .... time projection chambers, page 10
TPMon .... temperature and pressure monitor, page 20
TTL .... transistor-transistor logic, page 28

List of Figures

List of Tables

Bibliography

[1] W.-M. Yao *et al.*, *Review of Particle Physics*, Journal of Physics G: Nuclear and Particle Physics, *vol. 33*(1):1–1232, 2006.

[2] W. Cottingham and D. Greenwood, *An Introduction to the Standard Model of Particle Physics*, Cambridge University Press, 2007, 2nd ed.

[3] F. Halzen and A. D. Martin, *Quarks and Leptons: An Introductory Course in Modern Particle Physics*, John Wiley & Sons, Inc., 1984.

[4] D. H. Perkins, *Introduction to High Energy Physics*, Cambridge University Press, 2000, 4th ed.

[5] G. Abbiendi, *Search for the Standard Model Higgs Boson at LEP*, Phys. Lett. B, *vol. 565*(hep-ex/0306033. CERN-EP-2003-011. CERN-L3-271):61–75, Mar 2003.

[6] S. Weinberg, *A Model of Leptons*, Phys. Rev. Lett., *vol. 19*(21):1264–1266, Nov 1967, doi:10.1103/PhysRevLett.19.1264.

[7] A. Salam, *Weak and Electromagnetic Interactions*, originally printed in Svartholm: Elementary Particle Theory, Proceedings Of The Nobel Symposium Held 1968 At Lerum, Sweden, Stockholm, 367–377, 1968.

[8] S. L. Glashow, J. Iliopoulos, and L. Maiani, *Weak interaction with lepton-hadron symmetry*, Phys. Rev. D, *vol. 2*:1285–1292, 1970.

[9] J. Brau, Y. Okada, and N. Walker, *ILC Reference Design Report vol. 1 - Executive Summary*, *Tech. Rep. arXiv:0712.1950*, Dec 2007.

[10] ATLAS Collaboration, *ATLAS Detector and Physics Performance Technical Design Report, 1 and 2*, *Tech. Rep. number:ATLAS-TDR-014/015;CERN-LHCC-99-014/015*, CERN, Geneva, 1999.

[11] TESLA Collaboration, *TESLA Technical Design Report, 1-6 - The superconducting electron-positron linear collider with an integrated x-ray laser laboratory*, *Tech. Rep. number:DESY-2001-011*, DESY, Hamburg, 2001.

[12] N. Phinney, N. Toge, and N. Walker, *ILC Reference Design Report vol. 3 - Accelerator*, *Tech. Rep. arXiv:0712.2361*, Dec 2007.

[13] T. Behnke, C. Damerell, J. Jaros, and A. Myamoto, *ILC Reference Design Report vol. 4 - Detectors, Tech. Rep. arXiv:0712.2356*, Dec 2007.

[14] H. Bethe, *Bremsformel für Elektronen relativistischer Geschwindigkeit*, Z. Phys., *vol. 76, issues 5*:293–299, May 1932, doi:10.1007/BF01342532.

[15] H. Bethe, *Zur Theorie des Durchgangs schneller Korpuskularstrahlen durch Materie*, Ann. d. Phys., *vol. 397, issues 3*:325–400, 1930, doi: 10.1002/andp.19303970303.

[16] F. Bloch, *Bremsvermogen von Atomen mit mehreren Electronen*, Z. Phys., *vol. 81*:363–376, 1933.

[17] E. Uehling, *Penetration of Heavy Charged Particles in Matter*, Ann. Rev. Nucl. Part. Sci., *vol. 4*:315–350, 1954, doi:10.1146/annurev.ns.04.120154.001531.

[18] R. M. Sternheimer and R. F. Peierls, *General Expression for the Density Effect for the Ionization Loss of Charged Particles*, Phys. Rev. B, *vol. 3*(11):3681–3692, Jun 1971, doi:10.1103/PhysRevB.3.3681.

[19] C. Grupen, *Particle Detectors*, Cambridge University Press, 1996.

[20] D. Green, *The Physics of Particle Detectors*, Cambridge University Press, 2000.

[21] M. Weber, *Simulationen zur Verwendung von GEM-Folien als Auslesemodul einer TPC*, Master's thesis, TPC Group Aachen, Oct 2003.

[22] W. Blum and L. Rolandi, *Particle Detection with Drift Chambers*, Springer-Verlag, 1994.

[23] B. Sitar, G. I. Merson, V. A. Chechin, and Y. A. Budagov, *Ionization Measurements in High Energy Physics*, Springer-Verlag, 1993.

[24] F. Sauli, *Principles of operation of multiwire proportional and drift chambers*, CERN, Geneva, 1977.

[25] S. Bachmann, A. Bressan, L. Ropelewski, F. Sauli, A. Sharma, and D. Mörmann, *Charge amplification and transfer processes in the gas electron multiplier. oai:cds.cern.ch:385380*, Nucl. lnstr. and Meth. in Phys. Res. A, *vol. 438*(CERN-EP-99-048):376–408, Apr 1999.

[26] B. Sobloher, *Simulationsstudien zu GEM-Folien für die Auslese einer TPC*, Master's thesis, TPC Group Aachen, Mar 2002.

[27] S. Lotze, *Ion Backdrift Minimisation in a GEM-Based TPC Readout*, Ph.D. thesis, TPC Group Aachen, Apr 2006.

[28] F. Sauli, *From bubble chambers to electronic systems: 25 years of evolution in particle detectors at CERN (1979-2004)*, Phys. Rept., *vol. 403-404*:471–504, 2004.

[29] M. Killenberg *et al.*, *Modelling and measurement of charge transfer in multiple GEM structures*, Nucl. lnstr. and Meth. in Phys. Res. A, *vol. 498, issue 1-3*:369–383, Feb 2003.

[30] U. Werthenbach, University of Siegen, private communication.

[31] B. Dostal, University of Siegen, private communication.

[32] R. Brun and F. Rademakers, *ROOT –An object oriented data analysis framework*, Nucl. lnstr. and Meth. in Phys. Res. A, *vol. 389, issues 1-2*:81–86, Apr 1997, see also `http://root.cern.ch/`.

[33] U. Werthenbach, University of Siegen.

[34] M. Schild, *Untersuchungen zur hochauflösenden γ-Radioskopie mit Silizium-Streifendetektoren*, Ph.D. thesis, University of Siegen, Dec 1994.

[35] Z. K. Silagadze, *A new algorithm for automatic photopeak searches*, Nucl. lnstr. and Meth. in Phys. Res. A, *vol. 376, issue 3*:451–454, Jul 1996.

[36] M. Morhac, J. Kliman, V. Matousek, M. Veselsky, and I. Turzo, *Background elimination methods for multidimensional coincidence gamma-ray spectra*, Nucl. lnstr. and Meth. in Phys. Res. A, *vol. 401, issue 1*:113–132, Dec 1997.

[37] A. Kube, University of Siegen, private communication.

[38] W. Walkowiak *et al.*, KASCADE-Grande Collaboration, *A FADC-based Data Acquisition System for the KASCADE-Grande Experiment*, IEEE Transactions on Nuclear Science, *vol. 53*:265, 2006.

[39] S. Over, *Development and commissioning of data acquisition systems for the KASCADE-Grande experiment*, Master's thesis, University of Siegen, Jun 2004.

[40] Y. Kolotaev, University of Siegen, private communication.

[41] S. Over, University of Siegen, private communication.

[42] S. W. Smith, *The Scientist and Engineer's Guide to Digital Signal Processing*, California Technical Publishing, 1999.

[43] J. Pereira, P. Girao, and A. Serra, *An FFT-based method to evaluate and compensate gain and offset errors of interleaved ADC systems*, Instrumentation and Measurement, IEEE Transactions on, *vol. 53*(2):423–430, Apr 2004, ISSN 0018-9456, doi:10.1109/TIM.2004.823321.

[44] R. Seibert, University of Siegen, private communication.

[45] J. Elbornsson, F. Gustafsson, and J.-E. Eklund, *Blind equalization of time errors in a time-interleaved ADC system*, Signal Processing, IEEE Transactions on, *vol. 53*(4):1413–1424, Apr 2005, ISSN 1053-587X, doi: 10.1109/TSP.2005.843706.

[46] A. Münnich, *Experimentelle Untersuchung von GEM-Auslesestrukturen für eine TPC*, Master's thesis, TPC Group Aachen, Oct 2003.

Acknowledgements

It is my great pleasure to thank the many people who made this thesis possible.
To begin with, I would like to thank my parents for supporting my higher education. Their constant encouragement helped me get through my difficult times.
I would like to acknowledge the constant support and guidance of my supervisor Prof. Dr. Peter Buchholz. I thank him for giving me several opportunities to learn and expand my knowledge. His extended support has helped me finish my master study in time. I am grateful to Prof. Dr. Markus Schumacher for accepting to be the co-reviewer of my thesis. I would also like to express my gratitude to Prof. Dr. Claus Grupen and Prof. Dr. Ivor Fleck for their assistance and advice.
A special thanks goes to Dr. Wolfgang Walkowiak for proofreading this thesis and providing me with valuable comments and suggestions. In spite of his busy schedule, he managed to find the time and the means to help me even while he was on the move or remotely located.
I would like to take the opportunity to thank Adrian Kube, Bernd Dostal and especially Yury Kolotaev and Rudolf Seibert for their friendliness, patience and understanding. Without their efforts the experimental setup would never have materialized. I am also grateful to Sven Over for sharing his knowledge of Linux device drivers that helped me in building my own data acquisition components.
I would like to express my personal gratitude to Holger von Radziewski and Thorsten Stahl who were always available for helping me even in their busiest of times. I thank all my colleagues for creating a lively working atmosphere.
Lastly, and most importantly, I wish to thank Dr. Ulrich Werthenbach for being a great colleague and a friend. I benefited highly from his knowledge and experience. He has been a tremendous help throughout my master study. I really enjoyed working with him on this project.

Erklärung

Hiermit erkläre ich, dass ich die vorliegende Masterarbeit selbständig verfasst und keine anderen als die angegebenen Quellen und Hilfsmittel benutzt, sowie Zitate und Ergebnisse anderer kenntlich gemacht habe.

Siegen	17/03/2008	Bakul Gaur
(Ort)	(Datum)	(Unterschrift)